Modeling and Analysis of Sediment Trapping Efficiency of Large Dams using Remote Sensing

*Nishani Moragoda[1], Sagy Cohen[1], John Gardner[2], David Muñoz[3,4], Anuska Narayanan[1], Hamed Moftakhari[3,4], Tamlin M. Pavelsky[5]

[1]Department of Geography, University of Alabama, Box 870322, Tuscaloosa, AL 35401, USA.
[2]Department of Geology and Environmental Science, University of Pittsburgh, Pittsburgh, PA, USA.
[3] Department of Civil, Construction and Environmental Engineering, University of Alabama, Box 870205, Tuscaloosa, AL 35401, USA
[4] Center for Complex Hydrosystems Research, The University of Alabama, Tuscaloosa, AL 35401, USA
[5]Department of Earth, Marine and Environmental Sciences, University of North Carolina, Chapel Hill, NC 27599

*Corresponding author: npmoragoda@crimson.ua.edu

Key points

Remote sensing-derived surface river sediment fluxes strongly align with depth-averaged river sediment fluxes with a simple adjustment factor

Reservoir sediment trapping efficiency (*Te*) was calculated using remote sensing sediment data to develop empirical CONUS and global *Te* models

Large reservoirs can have a wide range of *Te* values, and reservoir volume (reservoir capacity) does not necessarily determine *Te*

Abstract

Sediment trapping behind dams is currently a major source of bias in large-scale hydro-geomorphic models, hindering robust analyses of anthropogenic influences on sediment fluxes in freshwater and coastal systems. This study focuses on developing a new reservoir trapping efficiency (*Te*) parameter to account for the impacts of dams in hydrological models. This goal was achieved by harnessing a novel remote sensing data product which offers high-resolution and spatially continuous maps of suspended sediment concentration across the Contiguous United States (CONUS). Validation of remote sensing-derived surface sediment fluxes against USGS depth-averaged sediment fluxes showed that this remote sensing dataset can be used to calculate *Te* with high accuracy (R^2 = 0.98). *Te* calculated for 116 dams across the CONUS, using upstream and downstream sediment fluxes from their reservoirs, range from 0.3% to 98% with a mean of 43%. Contrary to the previous understanding that large reservoirs have larger *Te* and vice versa, these data reveal that large reservoirs can have a wide range of *Te* values. A suite of 21 explanatory variables were used to develop an empirical *Te* model using multiple regression. The strongest model predicts *Te* using five variables: dam height, incoming sediment flux, outgoing water discharge, reservoir length, and Aridity Index. A global model was also developed using explanatory variables obtained from a global dam database to conduct a global-scale analysis of *Te*. These CONUS- and global-scale *Te* models can be integrated into hydro-geomorphic models to more accurately predict river sediment transport by representing sediment trapping in reservoirs.

Keywords: Reservoir trapping efficiency, remote sensing, dams, suspended sediment, global modeling.

1. Introduction

Global fluvial sediment transport is vulnerable to a variety of stresses from human activities including land use changes, water diversions, and damming (Best, 2019; Lewis et al., 2013, Lu et al., 2013). Rivers respond to such stresses in numerous and complex ways, which can lead to various environmental consequences (Li et al., 2020). The construction of dams and impoundments for hydropower generation, flood control, irrigation, and water supply is among the greatest stressors to the connectivity and functionality of rivers (Verstraeten and Poesen, 2000; Vörösmarty et al., 2003; Zarfl et al., 2015). Currently, ~58,000 large dams (heights greater than 15 m) exist in the world with an additional ~3,700 dams that are either planned or under construction (Best and Darby, 2020; Mulligan et al., 2020; Syvitski and Kettner, 2011). These impoundments collectively account for a cumulative storage capacity of ~8300 km^3, which is equal to around one-sixth of the total annual river discharge to the world's oceans (Lehner et al., 2011a; Wada et al., 2016). Apart from retaining a large amount of sediment behind them, dams alter downstream flow regimes affecting sediment carrying capacities, and trigger bank erosion and riverbed incision driven by sediment starvation from upstream trapping (Best, 2019; Kondolf et al., 2014b; Schmidt and Wilcock, 2008; Williams and Wolman, 1984). These alterations also lead to coarsening of the substrate, changes in channel planform, and reductions in sediment-associated nutrients in downstream areas which could result in collapsed ecosystem functioning and impacts on the fisheries industry (Brandt, 2000; Syvitski, 2003; Wohl and Rathburn, 2003). Construction of dams without assessing their potential consequences has led to degraded floodplain and coastal settings around the world (Latrubesse et al., 2017). In addition, reservoir sedimentation which is the most important factor affecting the utility and sustainability of reservoirs, depends on the trapping efficiency of the dam impoundment (i.e., the proportion of the incoming sediment load trapped in a reservoir) (Jothiprakash and Vaibhav, 2008). Reservoir sedimentation is a severe problem around the world, affecting water resources management (Kondolf et al., 2014a; Tan et al., 2019). Reservoir maintenance costs, flood control capacity, water treatment and distribution strategies, and water availability for domestic and agricultural uses can also be affected by the trapping efficiency of the reservoir.

Dams have caused a major reduction in the sediment loads in many of the world's rivers (Haddeland et al., 2014; Wei et al., 2021; Wu et al., 2020). The Huang He River in China, that

once had the highest river sediment flux in the world, is now experiencing diminished water and sediment flows reaching the coast, in part due to the numerous small and large dams constructed throughout its watercourse (Wu et al., 2020). The construction of the Hoover dam caused a large reduction of sediment flux in the Colorado River from about 125 MT/y to 3 MT/y (Williams and Wolman, 1984). Another widely cited example is the Aswan High Dam in the Nile River that reduced a pre-dam sediment load of 100 MT/y to nearly zero, causing a rapid shrink in the Nile River delta (Chakrapani, 2005; Walling, 2012). It has been estimated that approximately 26% (25-30%) of the global sediment flux is trapped in large reservoirs (Syvitski and Milliman, 2007, Syvitski et al., 2005; Syvitski et al., 2022; Vörösmarty et al., 2003).

Accurate estimation of reservoir trapping is vital for a variety of applications such as, accurately predicting river sediment transport, quantifying the global sediment delivery into the ocean, coastal/marine and deltaic environments, understanding anthropogenic influences on riverine fluxes, simulating future or theoretical change scenarios, evaluating ecological impacts, and informing dam operations (Merritt et al., 2003; Cohen et al., 2014; Dunn et al., 2019). Representation of sediment trapping by dams is currently a major source of bias in continental- and global-scale hydro-geomorphic modeling frameworks (e.g., Cohen et al., 2013). Several methods have been developed and tested over the years to estimate reservoir trapping efficiency (e.g., Brown, 1943; Churchill, 1948; Brune, 1953; Chen, 1975; Vörösmarty et al., 2003; Borland, 1971; Heinemann, 1984; Verstraeten and Poesen, 2000). The most widely used and adopted approach is Brune (1953) method where reservoir capacity to inflow ratio is considered in place of capacity to watershed ratio as previously suggested by Brown (1943). The Brune method was developed using 40 normally ponded and 4 other types of reservoirs, whereas the Brown method was based on data from 15 reservoirs. The Brune method was later modified by USDA-SCS (1983) to include particle size information. They suggested adjustments for dry reservoirs depending on sand or fine-textured nature of the sediment (Verstraeten and Poesen, 2000). In contrast, the Churchill (1948) curve calculates a ‘sedimentation index’ for the reservoir using residence time of water and flow velocity. It is applicable for reservoir types such as desilting and semi-dry which are different from normally ponded reservoirs. The Chen (1975) method predicts trapping for different particle size classes using flow velocity and particle size data. Rausch and Heinemann (1975) developed an equation that predicts reservoir trapping using

reservoir detention time, peak inflow rate (in place of inflow sediment particle size), storm runoff volume, sediment yield from storm, reservoir storage capacity, and drainage area. This regression equation, however, was developed using data from only three reservoirs in the Missouri River for individual storms and was not recommended for reservoirs with different characteristics. Verstraeten and Poesen (2000) also agreed that trapping efficiency depends on the inflow sediment characteristics and the water retention time of the reservoir, which in turn are controlled by reservoir geometry and runoff characteristics.

There are numerous factors that may govern variations in sediment trapping by dams. These may include local climatic, soil, topographic, and geologic conditions, in addition to characteristics of the river and dam impoundments. The volume of the reservoir relative to inflowing discharge, type and properties of the dam and reservoir, and sediment properties have been identified as key variables that govern sediment trapping in individual reservoirs (Brune, 1953; Heinemann, 1984; Kummu et al., 2010). For example, channel bed sediment composition may be a determining factor of sediment trapping owing to its erodibility and availability of fine/coarse sediment in the watercourse. Particle size of the incoming sediment flow was found to be an influencing factor that determines trapping efficiencies by many researchers (Rausch and Heinemann, 1975; Jothiprakash and Vaibhav, 2008). This also depends on the soils in the catchment and erosional processes (Verstraeten and Poesen, 2000). Larger particle sizes resulting from high intensity storm events yield high trapping efficiencies and vice versa. Therefore, if fine sediment dominates the watercourse, that may reduce trapping efficiency of the reservoir (Rausch and Heinemann, 1975). Regional climatic characteristics are also observed to have an influence on sediment trapping in reservoirs due to low mean annual flows in arid and semi-arid rivers compared to humid rivers with the same capacity to inflow ratio (Brune, 1953). Rausch and Heinemann (1975) suggested that factors such as reservoir capacity below the lowest spillway intake, length of reservoir, and depth through which particles must settle to be trapped may also affect trapping efficiency. Water retention time of the reservoir also depends on geometric characteristics of the reservoir such as storage capacity, shape, surface area, and outlet and spillway location (Jothiprakash and Vaibhav, 2008). In addition, runoff and discharge characteristics can affect trapping (Verstraeten and Poesen, 2000). Therefore, developing

accurate empirical models for estimating reservoir trapping efficiencies requires a comprehensive evaluation of globally available parameters such as those mentioned above.

Many large-scale sediment transport models currently rely on the approach of Vörösmarty et al. (2003) to calculate trapping as a function of local residence time change, an approximation of the Brune (1953) method. This method is convenient to use in large-scale models due to its simplicity and low input data requirement. These simplifications, however, can lead to increased bias and uncertainty. In addition, these methods have been developed using a limited number of dams in selected regions, and therefore, may not apply to reservoirs with different flow regimes and sediment production (Verstraeten and Poesen, 2000). There are a few reported instances where these methods significantly overestimated or underestimated trapping efficiency in reservoirs (e.g., Espinosa-Villegas and Schnoor, 2009; Lewis et al., 2013), however, to our knowledge, no large-scale comparison between measured and estimated sediment trapping efficiencies in individual reservoirs and dams have been reported in the literature. In order to calculate trapping efficiency using in situ measurements, long-term observations of sediment fluxes both upstream and downstream of a reservoir are needed, which are extremely rare.

Monitoring of river sediment loads by traditional field methods only provides point measurements at the gaging station and has limited spatial and temporal coverage (Cohen et al., 2013; Fagundes et al., 2020). These methods are also costly to establish and maintain and therefore, ongoing sediment monitoring programs worldwide are increasingly being terminated (Syvitski et al., 2005). Gaging stations for calculating sediment trapping are typically located far upstream and/or downstream of dams, which can introduce considerable errors to the trapping efficiency calculations (Brune, 1953). Given these limitations, traditional field methods do not provide sufficient data points to calculate incoming and outgoing sediment at reservoirs nor continuous data to construct longitudinal sediment profiles along rivers at large spatial scales. Numerical methods are increasingly being developed to simulate spatially and temporally distributed sediment dynamics in fluvial systems, however, providing accurate estimates of sediment loads still remains challenging due to our limited knowledge of the numerous interconnected processes that govern sediment dynamics and the difficulties in representing these complexities in models (Pelletier et al., 2012; Vercruysse et al., 2017). Sediment or turbidity rating curves are another option to obtain sediment data upstream and downstream of reservoirs,

but the relationship between discharge and sediment/turbidity is highly complex and varies in both time and space, and therefore prone to errors (Wang et al., 2021a).

Emerging remote sensing methodologies and datasets of fluvial sediment (Dethier et al., 2020; Gardner et al., 2021; Overeem et al., 2017; Yang et al., 2022) provide a unique opportunity to quantify, analyze, and model sediment trapping and its downstream impacts at continental and global scales. Remote sensing can also provide temporal dynamics, which is important as sediment trapping and its downstream impacts can vary over time (Rausch and Heinemann, 1975). Longitudinal sediment profiles developed using remote sensing data also provide opportunities to study spatial and temporal recovery patterns of the river system downstream of a dam.

This paper is focused on the development of conceptual understanding and parameterization of sediment trapping efficiency of large dams and exploring sediment dynamics downstream of dams. A novel reservoir trapping efficiency empirical model is developed using a new remote sensing dataset (Gardner et al., 2022) that offers high-resolution and spatially continuous suspended sediment concentration (SSC) data across the Contiguous United States (CONUS) for 1984-2018. This is the first dataset of its kind that enables the observation and modeling of fluvial suspended sediment dynamics at a continental scale, a transformative capability considering the scarcity in sediment gaging. Suspended sediment loads upstream of a reservoir and downstream of its dam are used to calculate sediment trapping in 116 reservoirs. These reservoir trapping data are used to develop a new reservoir trapping efficiency empirical model using widely available fluvial, environmental, and dam attributes. This analysis provides insights into the factors controlling the magnitude of suspended sediment trapping by dams at large spatial scales. In order to develop these quantitative relations, we employ statistical approaches such as multiple regression as well as machine learning techniques. We developed an additional model based on a global dataset of dams to extend our estimation of sediment trapping globally, providing a unique attribute for future analyses and modeling efforts. We also discuss the changes in suspended sediment loads downstream of dams using longitudinal sediment profiles extracted from the remote sensing dataset.

2. Methods

2.1. Dam selection and trapping efficiency calculation

The remote sensing sediment dataset used in this study was developed by Gardner et al. (2022), using Landsat 5, 7, and 8 processed in Google Earth Engine (GEE) and Machine Learning to convert imagery to SSC, generating high-resolution and spatially continuous maps of long-term averaged (1984-2018) SSC across the CONUS. This approach provides SSC (mg/L) data linked to the National Hydrography Dataset (NHDplus V21) river network (McKay et al., 2015). For more information about this data product and its validation, readers are referred to Gardner et al. (2021) and Gardner et al. (2022).

For this study, we calculated long-term averaged suspended sediment flux (kg/s) for each NHDPlus river reach by multiplying its remote sensing-derived SSC (mg/L) and NHDplus mean annual discharge (m^3/s). We used suspended sediment flux to calculate trapping efficiency instead of SSC to mitigate issues of water extraction and loss in reservoirs due to irrigation and evaporation, which can skew the calculation. For example, low sediment loads can be indicated as high sediment concentrations if a significant amount of water is extracted and removed from the system. Therefore, it is important to use flux values when calculating reservoir trapping even if it introduces an additional source of bias from the NHDplus discharge estimates.

We conducted a validation of the calculated suspended sediment flux values, and the NHDplus discharge values used to calculate them, against USGS gage sediment flux and water discharge data, respectively. The main objective of the validation was to find how well suspended sediment flux calculated by remote sensing-derived surface SSC represents the total, depth-integrated suspended sediment load of the river. The validation was conducted for 36 USGS gage sites where daily suspended sediment discharge measurements were available over the same period of time, and for sites located on the river network for which remote sensing data were available (Supplementary Table S1). However, the temporally-averaged USGS sediment flux values for some gaging stations do not represent the entire period of the remote sensing data. Based on this validation of suspended sediment flux, we introduced a simple adjustment factor to match the remote sensing-calculated surface suspended sediment fluxes to depth-averaged suspended sediment fluxes.

For the CONUS-scale analysis, we used the National Inventory of Dams (NID) dataset, published by the U.S. Army Corps of Engineers (https://nid.sec.usace.army.mil/ords/). The NID consists of more than 91,000 dams with attributes such as dam storage, dam height, dam length, drainage area, surface area of the impoundment, dam history, inspection, and hazard potential. We conducted an initial filtering to extract the dams located on the river network for which remote sensing sediment data were available, and have valid (non-zero) values for reservoir storage, drainage area, dam height, and dam length. Then through a meticulous manual procedure involving ArcGIS base maps, Google Earth, USA detailed water bodies layer package (ESRI, 2021), Global Reservoir and Dam (GRanD) Database (Lehner et al., 2011b), and NHDWaterbody layer, the locations of dams and reservoirs that correspond to the river network with remote sensing data were extracted. This resulted in 412 dams in total that are distributed across the CONUS. 189 cascading dams (where the next dam impoundment starts immediately or closely after the upstream dam) were removed from trapping efficiency calculations. However, we propose that cascading dams need to be further explored in the future to understand their role in sediment trapping and develop better models for predicting their *Te*. In this study, it was not realistic to calculate *Te* for cascading dams using remote sensing data as the incoming and outgoing river reach features for cascading dam impoundments mostly fall within the reservoir polygons.

Sediment trapping efficiency (*Te*; %) for individual dams was calculated as:

$$Te = \frac{Q_{s\_in} - Q_{s\_out}}{Q_{s\_in}} * 100 \quad (1)$$

where, Q_{s_in} is the suspended sediment flux entering the reservoir (kg/s), and Q_{s_out} is the suspended sediment flux immediately downstream of the dam. If there are multiple river reaches entering the reservoir, Q_{s_in} is equal to the sum of suspended sediment flux from all these reaches depending on data availability. For most of the dams, however, remotely sensed suspended sediment data were not available for all river reaches entering the reservoir.

Therefore, the incoming sediment flux into the reservoir may be underestimated, leading to conservative (underestimated) *Te* values.

Out of the 412 dams, 105 yielded negative *Te* values because outgoing sediment fluxes were greater than incoming sediment fluxes, indicating that these dams do not trap any sediment. The reasons for a negative *Te* may include (i) remotely sensed data capture the channel/bank erosion that occurs immediately after the dam, (ii) large tributaries that join the reservoir or the river reach immediately after the dam bring large amounts of sediment, (iii) lack of remote sensing sediment data for some of the incoming river reaches into the reservoir, (iv) dams use mechanisms to release sediment downstream, (v) bias in remote sensing sediment data, and (vi) in a few instances, the NHDplus river reach feature upstream of the reservoir, or downstream of the dam captures a part of the reservoir.

Further investigation into the 105 dams that yielded negative *Te* values (indicating no sediment trapping) revealed that the main purpose of the dam may play a role in determining sediment trapping. Many dams with negative *Te* values in our dataset belong to those with a primary purpose of navigation and hydropower generation. Out of the 30 dams that had navigation designated as their primary use, 28 indicated no sediment trapping, whereas out of the 80 dams that had hydroelectricity designated as their primary use, 37 indicated no sediment trapping. On the contrary, dams built with the main purpose of irrigation, water supply, or flood risk reduction had only a few dams with zero *Te* values. However, it should be noted that many of these dams have multiple uses. This observation is reasonable as navigational dams or lock and dam structures are usually designed to release water, and thus sediment, downstream. Dams built for hydroelectricity, particularly run-of-river hydroelectric dams have little or no water storage and thus natural seasonal river flows are less obstructed. In contrast, dams and reservoirs built for water use purposes such as irrigation and water supply need to store the water. Taking this distinction into consideration, all dams with ‘navigation’ designated as their primary purpose were considered as having zero *Te*. However, no information was available in the NID dataset to distinguish run-of-river hydroelectric dams from conventional hydropower dams with impoundments. Therefore, all the hydropower dams with positive *Te* values were included in the

dataset. After removing cascading dams, dams with a negative *Te*, and navigational dams, 116 dams were available for use in the analysis (Figure 1).

A potential problem associated with calculating *Te* using remotely sensed upstream and downstream sediment loads is that Q_{s_out} captures the erosion taking place in downstream reaches. Therefore, the amount of sediment trapped may be higher than the calculated *Te.* This is, however, also an issue for calculating trapping using gage data from upstream and downstream of the reservoir, which is the standard method to calculate observed trapping efficiencies of dams.

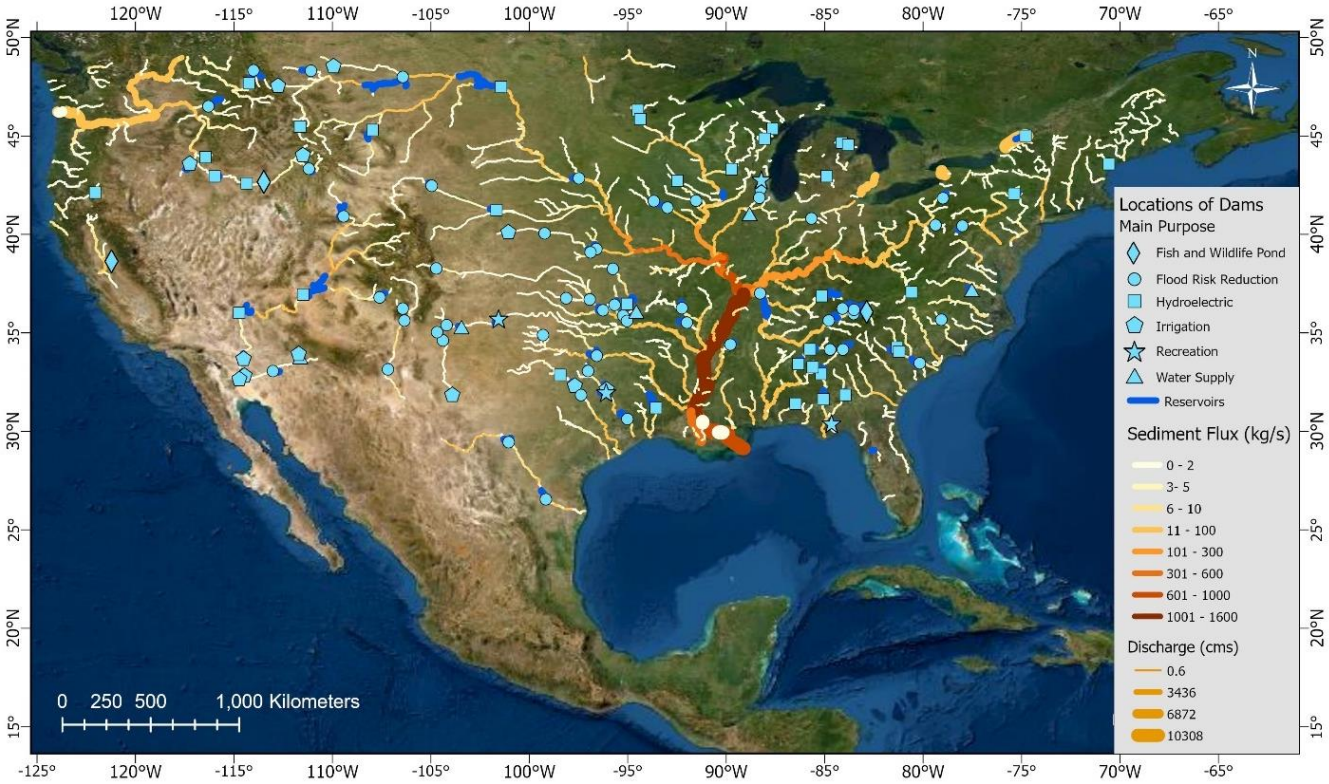

Figure 1: Map of the locations of 116 dams and reservoirs used in the analysis along with the river sediment fluxes calculated using the remote sensing data.

2.2. CONUS *Te* Model Development

Several environmental, fluvial, and dam-related variables that are widely available were collected to develop a CONUS-wide empirical *Te* model (Table 1). In addition to dam attributes provided by the NID dataset, we extracted fluvial, environmental, and dam attributes from the following geospatial datasets: NHDplus river network, Global River Width Dataset (Lin et al.,

2020), Reservoir Morphology Database for the Conterminous United States (Rodgers, 2017), Free Flowing Rivers dataset (FFR; Grill et al., 2019), GRanD database (Lehner et al., 2011b), GlObal geOreferenced Database of Dams (GOODD; Mulligan et al., 2020), and GeoDAR global reservoir and dam dataset (Wang et al., 2021b) with attributes acquired from the World Register of Dams (WRD) maintained by the International Commission on Large Dams (ICOLD; https://www.icold-cigb.org). Reservoir length along its longest part was calculated along the NHDplus river network using reservoir polygons. The relationship between these variables and *Te* was analyzed using multiple regression and machine learning. We used machine learning techniques, such as Random Forest Regression and Artificial Neural Network (e.g., Multi-layer Perceptron) models, with an 80% and 20% split of data for training and validation, respectively. Sensitivity and variable selection analyses (e.g., Variance Inflation Factor) were conducted to identify the key attributes that contain the largest variance of the data. In addition, we also applied Geographically Weighted Regression (GWR) to the dataset to identify local spatial variations in the relationship between explanatory variables and *Te*.

Table 1: Explanatory variables tested for developing the *Te* parameter

Variable	Symbols	Data type	Data source*
Incoming sediment flux	*Qs_in*	Line	Gardner et al. (2022)
Incoming discharge	*Q_in*	Line	NHDplus V21
Outgoing discharge	*Q_out*	Line (NHDplus), point (GRanD)	NHDplus V21, GRanD
Dam length	*D_Length*	Point	NID, GRanD
Dam height	*H*	Point	NID, GRanD
Reservoir storage	*S*	Point	NID, GRanD
Reservoir surface area	*SA*	Point	NID, GRanD
Drainage area	*D*	Point	NID, GRanD
Slope	*Slp*	Line	Lin et al. (2020)
Elevation	*Elev*	Line (Lin), point (GRanD)	Lin et al. (2020), GRanD
% Sand	*Snd*	Line	Lin et al. (2020)
% Silt	*Slt*	Line	Lin et al. (2020)
% Clay	*Cly*	Line	Lin et al. (2020)
Sinuosity	*Sin*	Line	Lin et al. (2020)
Aridity Index	*AI*	Raster (~1 km)	Lin et al. (2020), Trabucco and Zomer (2019)
Leaf Area Index	*LAI*	Line	Lin et al. (2020)

Sum of soil erosion from within the river reach catchment	*E*	Line	Grill et al. (2019)
2-yr return period flood	*Q2*	Line	Lin et al. (2020)
Dam age	*A*	Point	NID, GRanD
Lake length	*L*	Line	Grill et al. (2019)
Reservoir Depth	*Depth*	Point	GRanD

325

326 **2.3. Calculation and Analysis of a Global *Te* Dataset**

327 To enable a global-scale analysis, we also developed a global empirical *Te* model using dam
328 attributes from the GRanD database (Lehner et al., 2011b). In addition to the observed *Te* values
329 for the 116 US dams, observed *Te* was calculated for 4 dams in the Amazon Basin using a
330 similar remote sensing dataset (Narayanan, 2022). Observed *Te* for 36 dams in China (Hu et al.,
331 2009; Tan et al., 2019), the Bhakra Dam in India (Jothiprakash and Vaibhav, 2008; Sharma et al.,
332 2018), and the Aswan High Dam in Egypt (Biswas and Tortajada, 2012) were derived from the
333 literature. Thus, a total of 158 observed *Te* values were used to develop this global *Te* model.
334 Some of the missing explanatory variable data for these 158 dams in GRanD were substituted
335 with data from the NID dataset, or the GeoDAR global reservoir and dam dataset (Wang et al.,
336 2021b) with attributes acquired from the World Register of Dams (WRD). We then applied the
337 global *Te* model to the entire GRanD dataset to conduct global- and continental-scale analyses.
338 Some of the missing dam height data in GRanD were substituted using the GeoDAR dataset and
339 ICOLD attributes. For this global-scale application, reservoir lengths were calculated using an
340 automated process involving the Grill et al. (2019) river network and GRanD reservoir polygons.
341 GRanD dams that had missing data for essential explanatory variables, and dam impoundments
342 that did not fall on the Grill et al. (2019) river network were excluded from the analysis, which
343 resulted in 6823 dams for this analysis. The GRanD dataset does not include a reservoir polygon
344 for individual dams such as barrages, diversions, or run-of-the-river hydropower stations, which
345 may not form reservoirs. For these dams, and dams with navigation designated as the main use in
346 the GRanD database, the *Te* was assigned as zero. This dataset is envisioned to provide a *Te*
347 parameter for large-scale hydrological and geomorphic modeling frameworks.

3. Results and Discussion

3.1. Evaluation of the Remote Sensing Sediment Data

A major limitation of remote sensing of sediment is that it can only capture sediment concentration for the top layer of the river water column. Existing theoretical methods to obtain depth-averaged sediment concentration profiles such as the Rouse profile require data on water depth, sediment settling velocity, shear velocity at different water depths, and other coefficients (Laguionie et al., 2007) which are not readily available. Blanchard et al. (2011) reported that suspended sediment concentration varied at different depths among different sites they measured. A universal method to estimate sediment concentration profiles using surface sediment fluxes has yet to be developed. We conducted a comparison between USGS measured and remote sensing-calculated sediment fluxes for 36 gaging stations. The results show that the remote sensing sediment flux is consistently underestimated (Figure 2b).

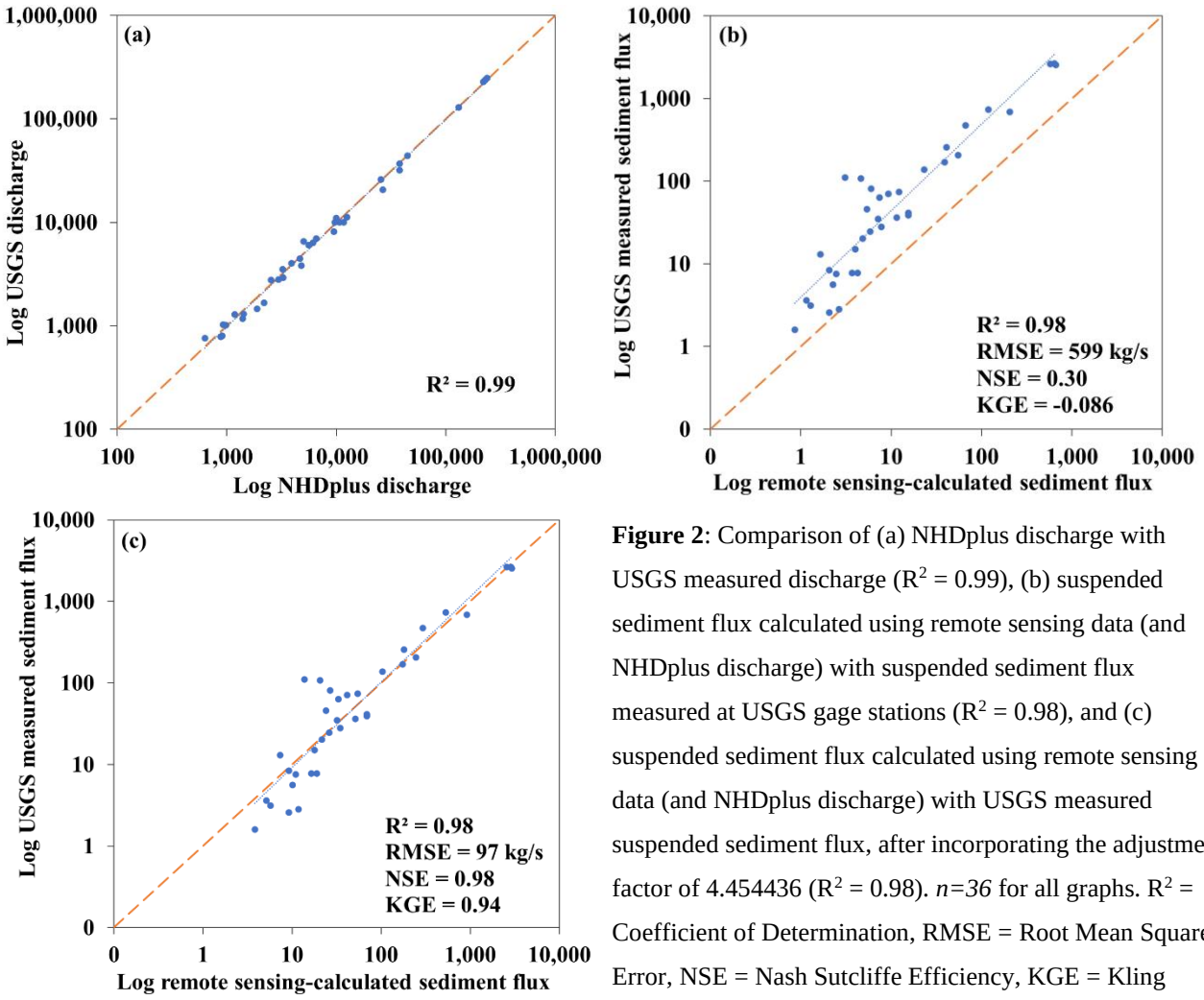

Figure 2: Comparison of (a) NHDplus discharge with USGS measured discharge (R^2 = 0.99), (b) suspended sediment flux calculated using remote sensing data (and NHDplus discharge) with suspended sediment flux measured at USGS gage stations (R^2 = 0.98), and (c) suspended sediment flux calculated using remote sensing data (and NHDplus discharge) with USGS measured suspended sediment flux, after incorporating the adjustment factor of 4.454436 (R^2 = 0.98). *n=36* for all graphs. R^2 = Coefficient of Determination, RMSE = Root Mean Square Error, NSE = Nash Sutcliffe Efficiency, KGE = Kling Gupta Efficiency.

A comparison between NHDplus discharge and USGS measured discharge shows that the discharge values correspond nearly perfectly to the in-situ measurements and, hence are highly reliable (Figure 2a). This may also be attributed to the fact that NHDplus mean annual discharge is gage adjusted based on the observed flow (Moore et al., 2019). NHDplus is, however, widely used in hydrological studies as a reliable source of mean annual discharge, so we are quite confident in these values throughout the CONUS. We can therefore conclude that the source of underestimation of the calculated sediment flux is that it reflects water surface suspended sediment concentration. A simple adjustment factor of 4.45 yields the strongest alignment with the 1:1 line, yielding the lowest sum of residuals and improved model performance statistics (RMSE, NSE, and KGE), so that sediment flux calculations are representative of the depth-averaged sediment flux in the in-situ observations (Figure 2c). This result shows that remote sensing-derived suspended sediment fluxes can be used to calculate *Te* with high accuracy using a simple adjustment factor. The efficiency of the uniform adjustment factor is surprising given the diversity of the gage locations, the range of sediment flux values (3 orders of magnitude), and the known complexity in the fluvial sediment-depth relationship. The strong linear fit in figure 2c implies that average surface suspended sediment flux is uniformly 4.45 times smaller than depth-averaged flux across a wide range of rivers over the CONUS. This finding merits further investigation using a wider geographical range. A smarter adjustment factor may be warranted to reduce the relatively high scatter observed for smaller values of sediment flux, though, more data would be required to develop such an adjustment factor.

3.2. Sediment Dynamics Along Longitudinal Profiles

The Missouri River is a great case study to examine the changes in sediment dynamics along its longitudinal profile due to obstruction by a diverse set of large dams (Figure 3). The largest of these dams in terms of reservoir capacity include the Garrison Dam forming Lake Sakakawea, Oahe Lake and Dam, and Fort Peck Lake and Dam, with reservoir storage capacities of 32.1 km^3, 29.1 km^3, and 23.6 km^3, respectively. As expected, both the sediment concentration and flux generally increase as the river flows downstream. The trends in sediment concentration and flux are generally similar. A rapid decrease in the sediment load (both concentration and flux) is observed within reservoirs (highlighted color sections in Figure 3b). This shows the deposition of

sediment in the reservoir due to reduced flow velocity (Verstraeten and Poesen, 2000). Near the headwaters of the Missouri River, sediment flux increases downstream at a rate of 0.05 kg/s/km, and then a steep decrease in sediment is observed once it reaches the first set of relatively small cascading dams (collectively account for 3.1 km^3 storage capacity). The sediment load increases without obstructions from large dams for about 493 km downstream at a rate of 0.27 kg/s/km. Once the river enters Fort Peck Lake, sediment load rapidly decreases at a rate of -0.52 kg/s/km due to deposition in the reservoir. Fort Peck Dam traps 93.6% of its incoming sediment flux as calculated by the remote sensing dataset. Sediment loads increase rapidly immediately after the Fort Peck dam due to the high sediment-yielding Milk River confluence (Figure 4).

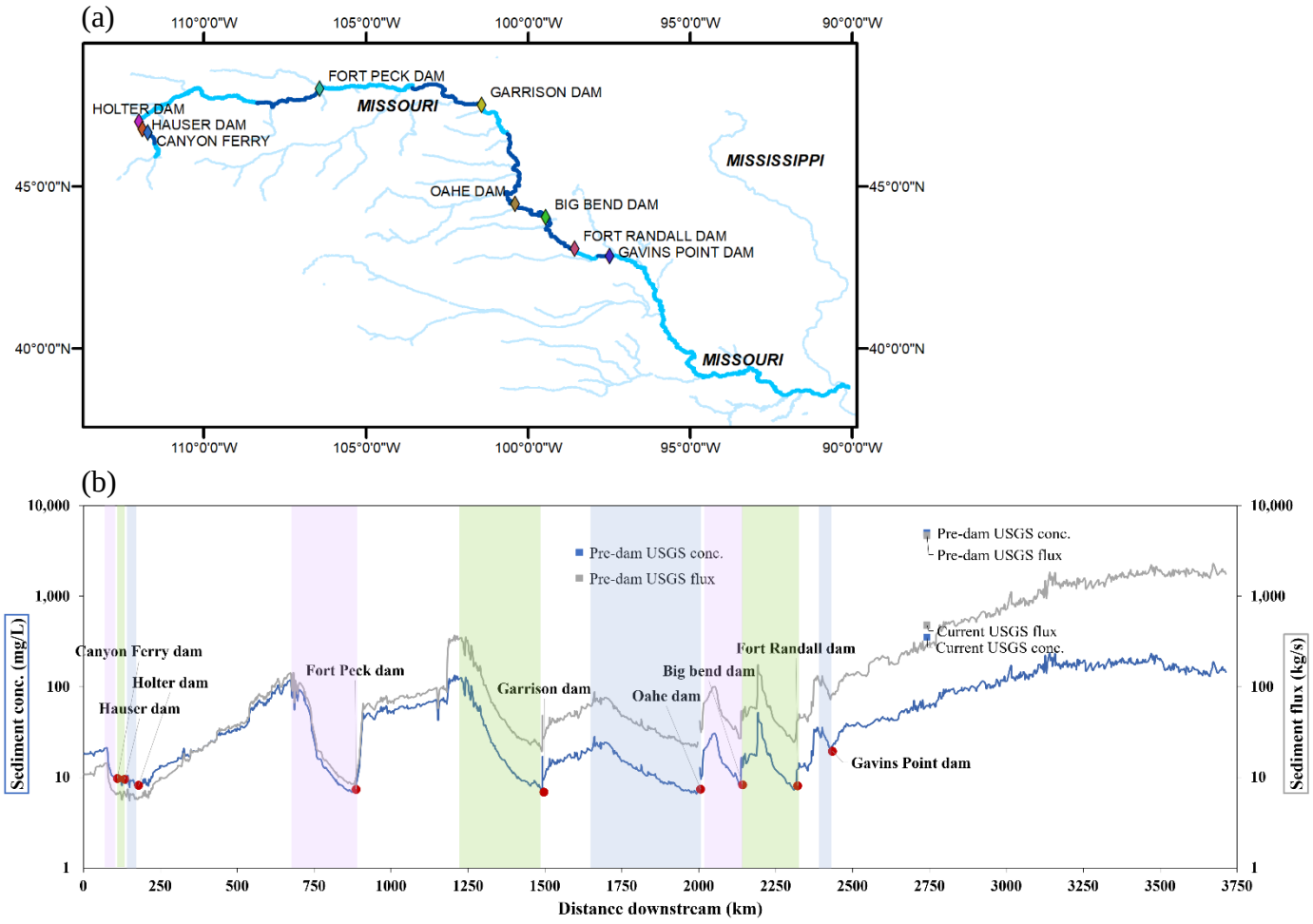

Figure 3: Longitudinal profile of sediment dynamics in the Missouri river. (a) Map of the Missouri River and its dams. (b) Trend in sediment concentration and flux along the Missouri River. The red dots show the dam locations, whereas the blue and grey lines show the sediment concentration (mg/L) and adjusted

sediment flux (kg/s) obtained from the remote sensing data, respectively. Pre-dam construction and current observed long-term average sediment concentrations (blue squares) and fluxes (grey squares) were calculated from USGS gage sites where data are available. The colored areas indicate the extent of reservoirs corresponding to the dams. Note that vertical axes are converted to log scale to enhance visualization.

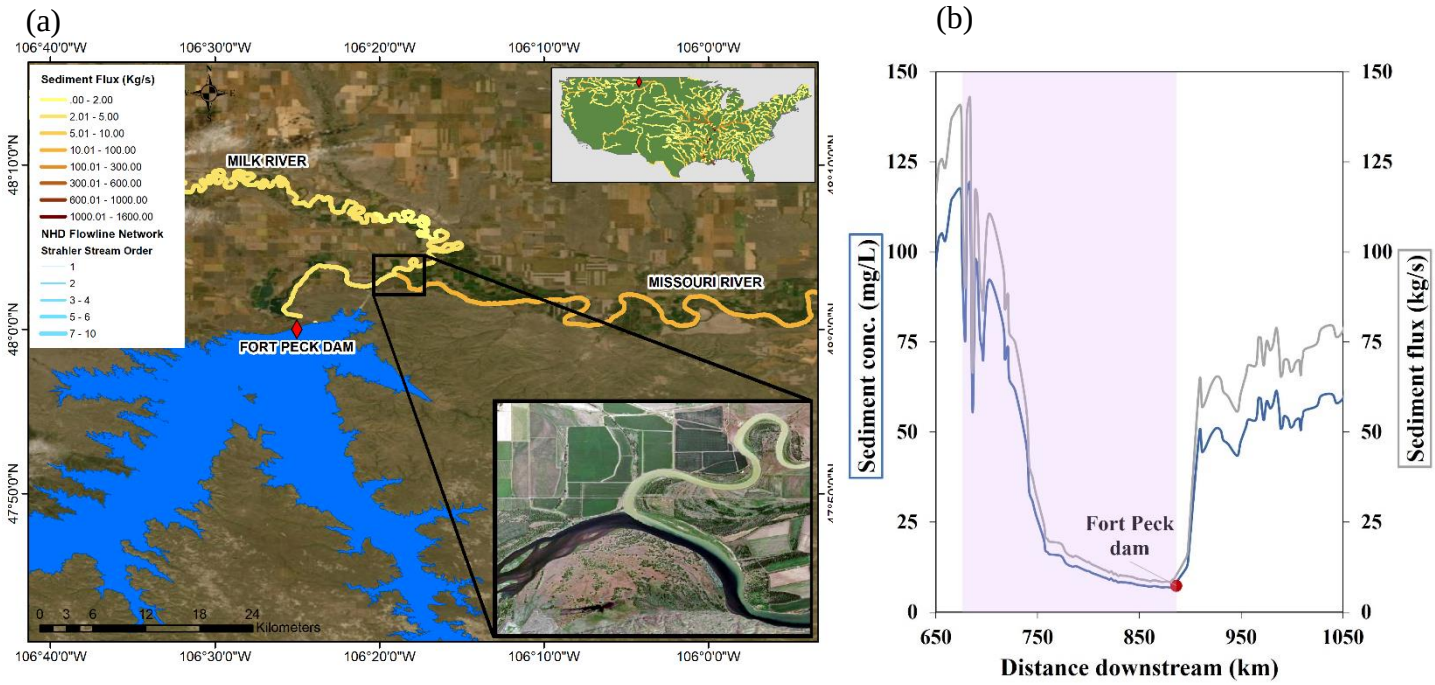

Figure 4: The Milk River joining the Missouri river immediately after the Fort Peck dam, contributing to a sudden increase in downstream sediment load. 5(b) shows the longitudinal sediment profile of the river segment with the colored bar showing the reservoir extent. Blue and grey lines show the sediment concentration (mg/L) and adjusted sediment flux (kg/s) obtained from the remote sensing data, respectively.

The next large dam along the Missouri profile, Garrison (km 1,500 in Figure 3b), traps 85.2% of its incoming sediment flux. The pattern of decrease in sediment within the reservoir length and a sudden increase in sediment after the dam can also be clearly observed at this location, as well as Oahe, Big Bend, and Fort Randall dams and reservoirs. The increase in sediment after the dam at Oahe, Big Bend, and Fort Randall dams are gradual increases within a short distance (as opposed to the sudden increase after Fort Peck) and can likely be attributed to both instream erosion and sediment influx from smaller tributaries. The spike after the Garrison dam could be due to the

turbidity at the start of the spillway. The spike in sediment flux and concentration at km 2,192 within Lake Francis Case (formed by the Fort Randall Dam) is due to the White River joining the Missouri river. The increase in sediment between Fort Randall dam and Lewis and Clark Lake (formed by Gavins Point dam) at 2,374 km downstream point is due to the Niobrara River joining the Missouri River. Gavins Point dam also shows a similar pattern of sediment trapping and a gradual increase downstream. Along its most downstream segment (~2,400 – 3,750 km), the Missouri River flows without dam obstructions until it joins the Mississippi River, gaining sediment along the way, with considerable contribution from tributaries. The rate of increase in sediment flux along this segment of Missouri is 1.32 kg/s/km.

USGS gage sediment concentration and flux data prior to dam construction were obtained for two locations along the Missouri River: Missouri River at Bismarck, ND at km 1,612 (USGS gage number: 06342500) and Missouri River at Omaha, NE at km 2,741 (USGS gage number: 06610000). The latter also provide post dam-construction measurements. For the Bismarck station, daily sediment data were available only for the year 1946, therefore, this was used to calculate the average sediment loads prior to dam construction. For the Omaha station, average prior-to-dam sediment concentration and flux were calculated using daily data for the period between 1939 – 1951, while current sediment concentration and flux were calculated using daily data for the period between 1991 – 2019 (excluding 2004 – 2007 due to missing data). The current sediment flux from USGS data at Omaha station (477 kg/s) compares reasonably well with the adjusted sediment flux from remote sensing data for this location (294 kg/s), considering the difference in the temporal range. The difference between the prior-to-dam and contemporary sediment fluxes observed at the gage site is over an order of magnitude at the Omaha station (4694 kg/s to 477 kg/s) and two orders of magnitude at the Bismarck station (1587 kg/s to 49 kg/s).

The Colorado River (Figure 5) is well known for its near-zero sediment flux to the ocean due to the high degree of sediment trapping by dams and water extractions. Sediment load increases at an average rate of 1.07 kg/s/km from the headwaters in Rocky Mountains National Park, CO, until km 620, downstream of which sediment load decrease, before entering the Glen Canyon reservoir (left-most highlighted section in Figure 5c). Glen Canyon Dam traps on average 95%

of the incoming sediment load, resulting in a near-zero load downstream. Until the river enters Lake Mead (formed by the Hoover Dam), sediment flux generally increases at an average rate of 0.84 kg/s/km. The areas with missing (and highly fluctuating) remote sensing-captured SSC before the start of Lake Powell (formed by the Glen Canyon Dam), as well as in river reaches between Glen Canyon dam and Lake Mead, are the portions of the Colorado River that flow through the Canyonlands National Park, and the Grand Canyon, respectively. These more confined segments of the river pose challenges for remote sensing techniques due to (1) generally very narrow river widths, (2) steep canyons creating hill shadows, (3) in areas where rapids/white water areas are interspersed with slow water flows, rapids may be indicated as high SSC, and (4) a number of small tributaries along this part of the river that deliver considerable amount of sediment to the Colorado River potentially contributing to the high variability.

The Hoover Dam traps 83.3% of the incoming sediment load, and the dams that follow such as Davis, Parker, Palo Verde diversion, etc. keep the sediment load from recovering. The Morelos diversion dam, which is the last dam on the Colorado River, diverts a large portion of its water for irrigating highly developed croplands in the Mexicali Valley, Mexico. The Colorado River has a very low water discharge from this point onwards (Figure 5b). Although the NHDplus river network and therefore sediment data ends at the Morelos diversion dam shortly before reaching the US-Mexico border, the river extends further until it reaches the ocean. This longitudinal river profile shows the dynamics leading to a very low sediment flux from the Colorado River to the ocean.

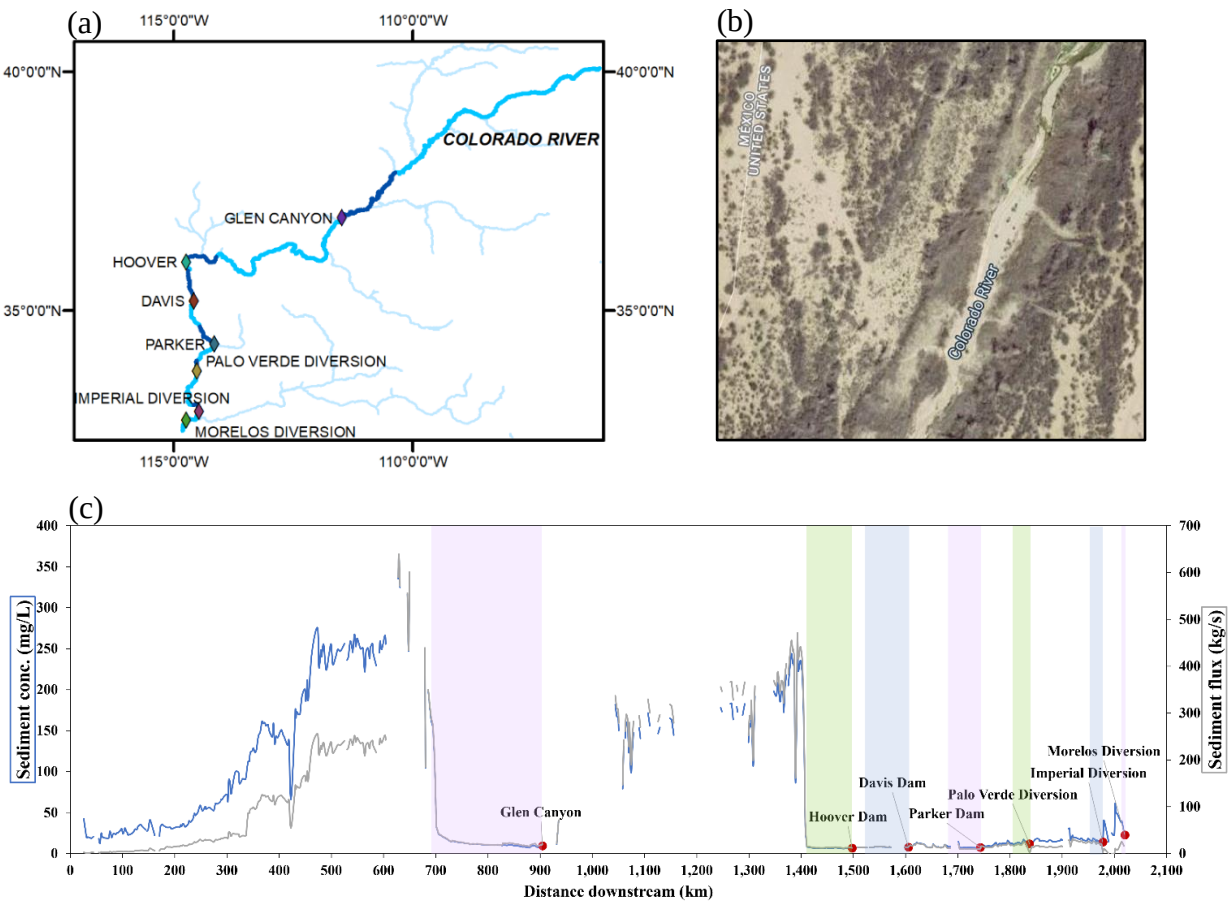

Figure 5: Longitudinal profile of sediment dynamics in the Colorado river. (a) Map of the Colorado River and its dams. (b) Colorado River after the Morelos Diversion Dam with very low discharge. (c) Mean sediment concentration and flux along the Colorado River. The red dots show the dam locations, whereas the blue and grey lines show the sediment concentration (mg/L) and adjusted sediment flux (kg/s) obtained from the remote sensing data, respectively. The colored areas indicate the extent of reservoirs corresponding to the dams.

Similar patterns in sediment trapping and downstream recovery are observed in other rivers (e.g., Figure 6(c) the Catawba and Wateree Rivers, Figure 6(d) the Tennessee River). In the Catawba and Wateree Rivers, clear decreases in sediment concentrations are observed at reservoir locations, however, this trend is not very prominent in sediment flux. This may be due to the gradual increase in discharge throughout the water course that alleviated the changes in sediment concentration until the Wylie dam (km 206). Sediment concentration and flux both increase for about 28 km downstream of Wylie dam at a rate of 0.33 kg/s/km until the next set of cascading

dams trap a large amount of sediment. Following these dams, a gain in sediment is observed until the Wateree River and Congaree River confluence, at a rate of 0.14 kg/s/km. In the Tennessee River (Figure 6d), although sediment concentration shows decreases at reservoir locations, sediment fluxes show a general increasing trend until the Kentucky Lake (km 846), despite multiple dam obstructions. Kentucky Dam shows a reduction in both sediment concentration and flux within the reservoir. The spikes in sediment within the lakes formed by the Wheeler dam and Kentucky dam are due to large tributaries. The spike immediately after Fort Loudoun Dam (km 80) is also owing to a tributary confluence.

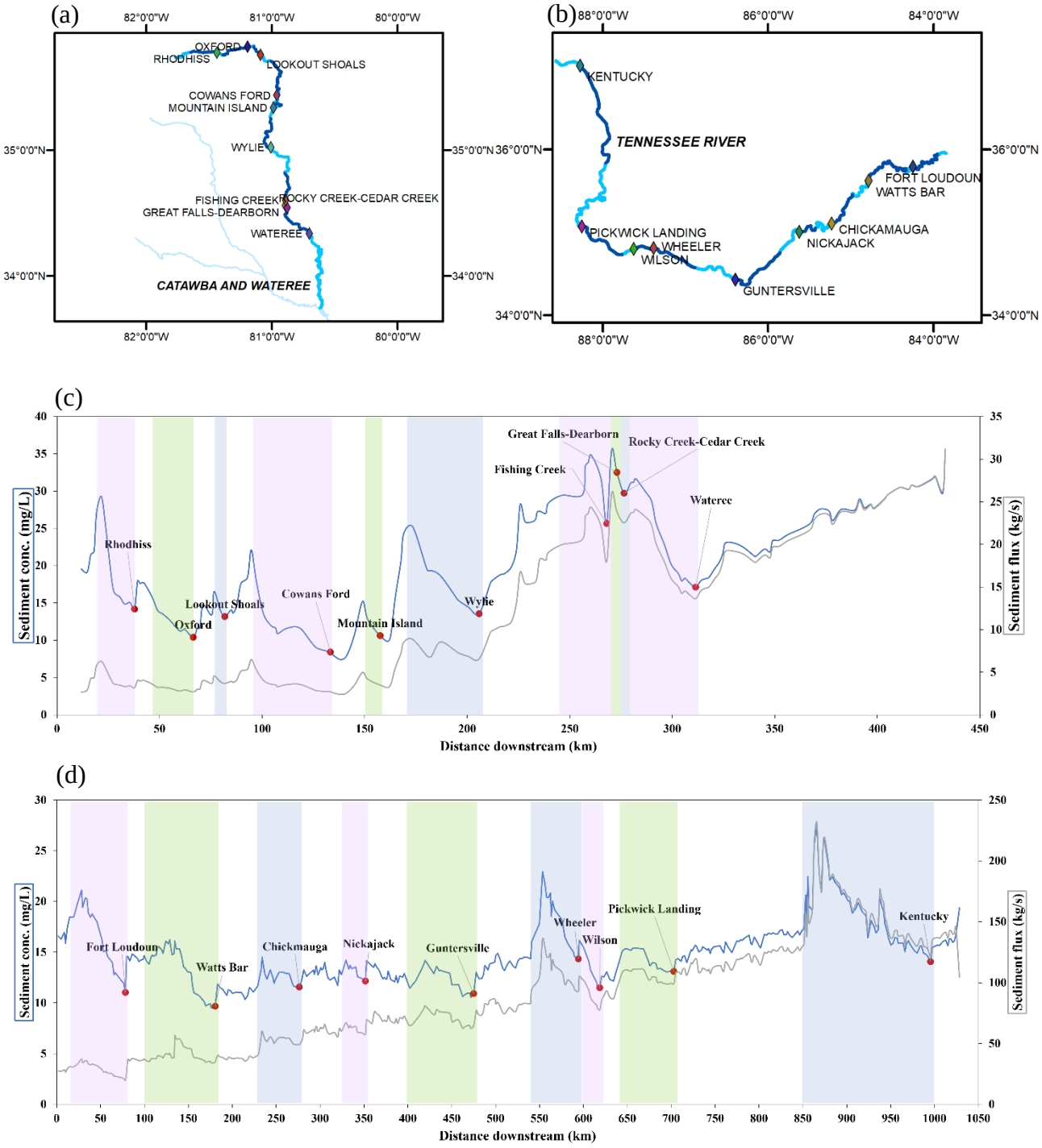

516

517 **Figure 6:** Longitudinal profile of sediment dynamics in the Catawba and Wateree and Tennessee Rivers.
518 Map of (a) Catawba and Wateree and (b) Tennessee Rivers with their dams. Trend in sediment
519 concentration and flux along the (c) Catawba and Wateree (d) Tennessee Rivers. The red dots show the
520 dam locations, whereas the blue and grey lines show the sediment concentration (mg/L) and adjusted

sediment flux (kg/s) obtained from the remote sensing data, respectively. The colored areas indicate the extent of reservoirs corresponding to the dams.

The longitudinal river sediment profiles constructed using the remote sensing data also reveal how the effect of trapping gradually decays downstream of dams. Increases (or replenishment) of sediment downstream of large dams can be attributed to several mechanisms: (1) increased transport capacity of the river flow, leading to channel scour, incision, and bank erosion ("hungry rivers"; Kondolf et al., 2014a; Kondolf et al., 2014b; Kummu et al., 2010), which was shown to rapidly increase sediment loads downstream (Brandt, 2000; Williams and Wolman, 1984), (2) large tributaries that drain sediment into the main river, (3) eroded soil from the surrounding areas of the river reach catchment, and (4) dams may have mechanisms to release sediment downstream. The relative proportions of downstream sediment recovery that can be attributed to these processes need to be quantified to better understand downstream sediment recovery processes. However, this remains challenging mainly due to lack of data on sediment flows in most major tributaries, limiting our ability to calculate the mass balance of sediment along river corridors.

3.3. Sediment Trapping Calculations for CONUS Dams

Reservoir *Te* calculated using remote sensing-derived adjusted sediment flux values (Eq. 1) for the 116 dams, range from 0.3% to 98% with a mean of 43% and a standard deviation of 27.8%. Figure 7 shows the spatial variability of the remote sensing-calculated *Te*. It can be observed that dams with the largest *Te* values are mostly located in the arid mid-west regions of the US, whereas dams in the Eastern and North-West parts of the country generally have lower *Te* values. This suggests that regional climate, particularly aridity, may be a factor that determines *Te*, or serve as a proxy for a combination of properties that are common for dams in arid regions. These properties may include sediment particle size, reservoir size and depth, and dam operations. Many of the dams in the arid mid-west have large reservoirs, and limited or no ability to release sediment. Also, the sediments in this region tend to be coarser and are, therefore, more rapidly deposited due to higher settling velocity, once reaching the reservoir (Verstraeten and Poesen, 2000). Many of the dams on Eastern US rivers are not necessarily designed for storage (rather for navigation, hydropower generation etc.), and therefore, tend to be shallower and/or

552 can be run-of-river dams. Also, suspended sediments in these regions tend to be finer, which
553 decreases their ability to be trapped. Vörösmarty et al. (2003) also found that dams in arid
554 regions tend to have larger *Te* values due to their highly variable discharge regimes, high demand
555 for water for irrigation and community water uses, and the resulting necessity to store water. The
556 effect of the aridity index was further explored using Geographically Weighted Regression when
557 developing the CONUS *Te* model, which is explained in section 3.4.
558

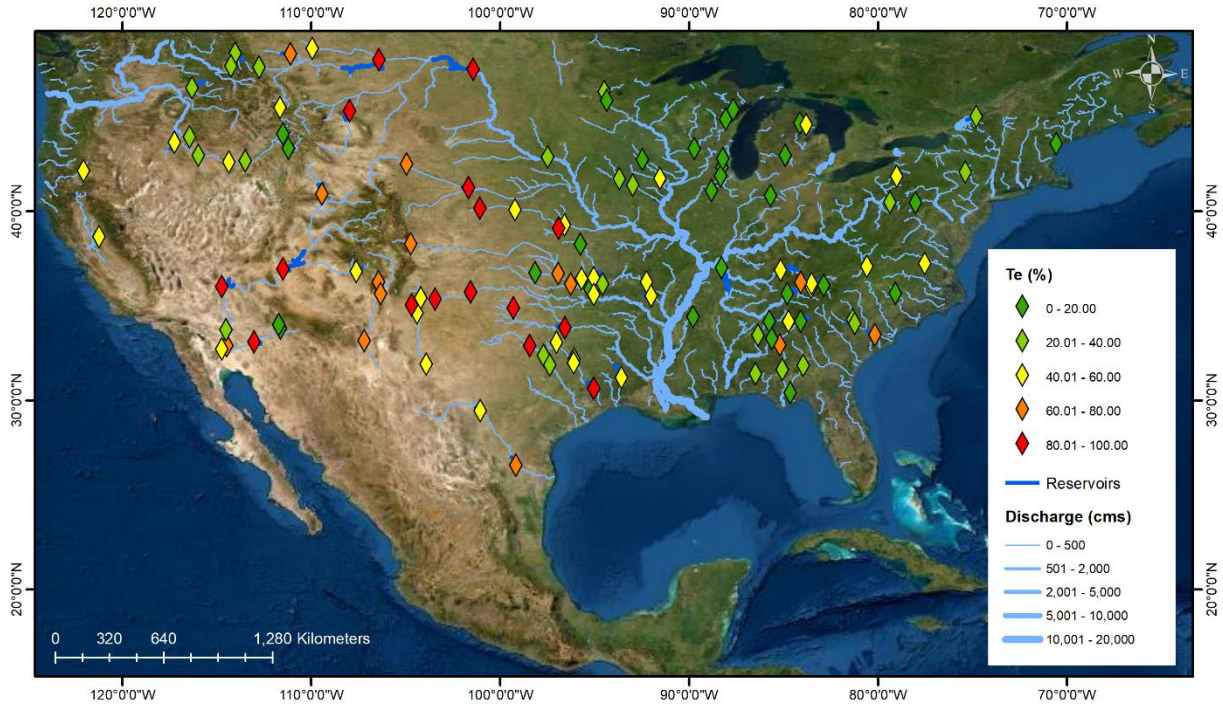

559 **Figure 7**: Trapping efficiency (*Te*; %) of the 116 dams calculated using observed remote sensing data.
560

561 The rate of decreasing sediment flux (sedimentation) within individual reservoirs was calculated
562 for all 116 dams using the amount of sediment trapped and the lake length along the longest part
563 of the reservoir. The 116 reservoirs studied here have a mean trapping rate of 0.27 kg/s/km,
564 ranging from 0.002 and 2.1 kg/s/km. The pattern of sediment decay within the reservoir length
565 varies across reservoirs, but generally follows an exponential shape, with sedimentation rates
566 decreasing along the reservoir downstream length (e.g., Figure 3b).
567

568 **3.4. CONUS *Te* Model**

Twenty one (21) explanatory variables were tested to predict reservoir *Te* using machine learning methods as well as multiple linear regression, based on the *Te* derived for the 116 dams. The list of explanatory variables used is provided in Table 1.

A multiple regression model was developed after confirming that the data meet the necessary assumptions for regression. The model yielded an R^2 of 0.68 (Adj. R^2 = 0.66) using five variables: dam height (log converted), incoming sediment flux (log converted), outgoing water discharge (log converted), reservoir length along the longest part, and Aridity Index. All these variables significantly contribute to the regression model ($p < 0.05$). This indicates that 68% of the variability in *Te* can be explained by these five variables with a Root Mean Square Error (RMSE) of 16.1% and a Nash Sutcliffe Efficiency (NSE) of 0.68. The resulting model equation is:

$$Te = 49.43 + 31.26\log(Q_{s\_in}) - 37.05\log(Q_{out}) + 19.68\log(H) + 0.15\,L - 13.81\,AI \quad (2)$$

where Q_{s_in} is the adjusted incoming sediment flux (kg/s), Q_{out} is the outgoing discharge (m^3/s), H is the dam height (m), L is the lake length along the longest part (km), and AI is the aridity index (higher values for humid regions) calculated for the reservoir polygon. The importance of the independent variables in the model in descending order based on the standard coefficients and contribution to change in the R^2, are Q_{out}, Q_{s_in}, H, L, and AI. Figure 8 shows the performance of the multiple linear regression model (Eq. 2) in predicting *Te*. Higher degree of scatter can be seen for low observed *Te*. Geographically Weighted Regression confirms a uniform distribution of Local R^2, and the maps of standard residual and standard error confirm a random distribution. This indicates a robust model and a consistent relationship between explanatory variables and observed *Te* in geographic space.

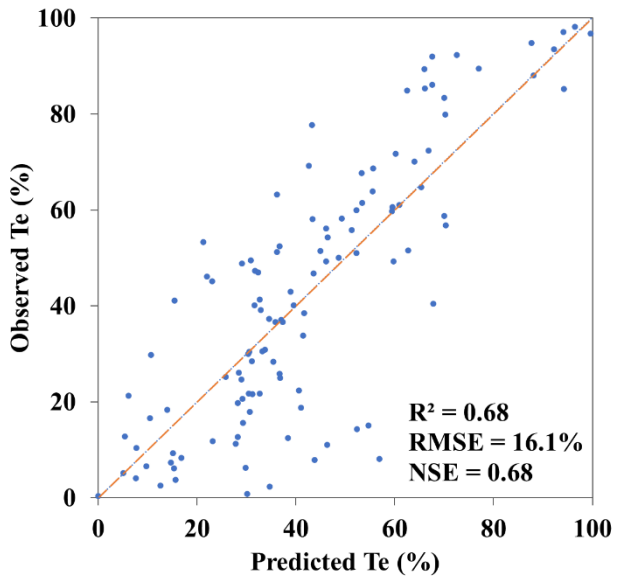

Figure 8: Evaluation of the *Te* predicted by the regression model (Eq. 2) and the *Te* calculated using remote sensing sediment data (*n =116*). The orange line is the 1:1 line. The trend line falls on the 1:1 line.

For comparison, we calculated *Te* for these US dams using the Brune (1953) formula for individual reservoirs, later adopted globally by Vörösmarty et al. (2003) and Syvitski et al., (2005). This is currently the most widely used approach to represent sediment trapping in large-scale sediment transport models. This method predicts *Te* for individual reservoirs as a function of local water residence time change, calculated as the effective reservoir capacity divided by local mean annual discharge. Figure 9 shows a comparison between *Te* calculated using Eq. 2 and the Brune (1953) formula for reservoirs with > 0.5 km^3 storage capacity (defined as large reservoirs by Vörösmarty et al. (2003)). Our *Te* model results in noticeably different values compared to the Brune (1953) approach. The most widely accepted idea about reservoir trapping efficiencies yielded by previous studies is that *Te* is very large for large reservoirs and small for small reservoirs. Williams and Wolman (1984) suggested that *Te* of large reservoirs are commonly greater than 99%. Vörösmarty et al. (2003) indicate that the *Te* of large reservoirs is typically ~85%. Contrary to these findings, our results show that reservoir volume (indicated by storage capacity) does not necessarily play an important role in determining sediment trapping. According to the remote sensing sediment data, large reservoirs can have a wide range of *Te* values. This may be partly due to the fact that Q_{s_out} is capturing the downstream erosion to

some degree, leading to an underestimation of *Te*. The longitudinal profiles constructed using remote sensing sediment data (section 3.2) show that the reduction in sediment is dramatic and consistent downstream in some dams, while it is not the case in others. This consistency of remote sensing SSC and flux downstream of the dams (for hundreds of km in some cases) is evidence of the robustness of the data and the methodology in capturing the net effect of a dam. Considering the possibility of under-predictions in *Te* due to erosion or remote sensing artifacts downstream of a dam, our *Te* results and model may be considered as representing the net reduction in sediment load due to damming (trapping – increase erosion). Capturing this net effect is particularly important for sediment modeling studies to represent the actual effect of dams and reservoirs in sediment trapping.

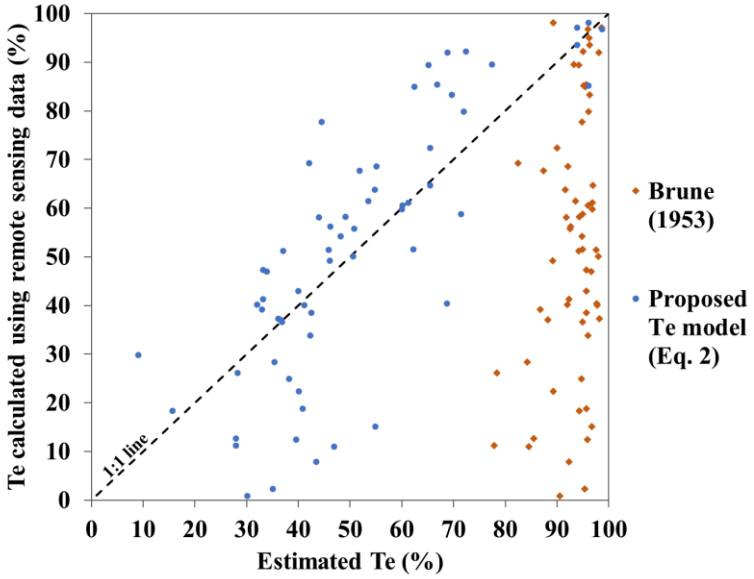

Figure 9: Comparison of *Te* calculated using the remote sensing data versus the proposed regression model (blue) and Brune (1953) method (red), for reservoirs with >0.5 km^3 storage capacity (*n=65*).

The model provides new insights into drivers of *Te*. The sediment flux entering the reservoir plays an important role in governing trapping within the reservoir and *Te* is higher for higher incoming sediment fluxes. A study that looked at reservoir trapping for individual storm events found that, for similar detention times (length of time runoff from a storm event remains in the reservoir), high incoming sediment loads had higher *Te* (Rausch and Heinemann, 1975). Rausch and Schreiber (1981) also predicted *Te* for Callahan Reservoir by storm detention time, total

storm runoff, and mean inflow sediment concentration. One criticism that conventional methods such as Brune (1953) receive is that they are developed for normally ponded reservoirs mostly located in temperate settings and do not yield accurate results for tropical rivers with highly variable inflows, desilting, or semi-dry reservoirs (Lewis et al., 2013; Verstraeten and Poesen, 2000). This may be because sediment trapping is highly influenced by the incoming sediment rates. The equations proposed here address this issue by incorporating sediment inflow to the reservoir as a predictor variable.

For lower rates of water discharge from the dam, *Te* is higher indicating less release of sediment and therefore, higher trapping values. The height of the dam is also included as a key variable indicating that taller or in general larger dams facilitate more trapping of sediment. Larger values of reservoir lengths provide sufficient time for sedimentation within the reservoir, leading to larger *Te* values. This parameter may be a proxy for sediment retention time of the reservoir which is widely used by methods such as Brune (1953) and Rausch and Heinemann (1975). Aridity index values obtained from Lin et al. (2020) which is originally based on Trabucco and Zomer (2019) indicates higher *Te* for dam impoundments in arid regions. This can also be clearly seen in the spatial distribution of *Te* shown in Figure 7. Further exploration of the influence of aridity on *Te* estimations using the Geographically Weighted Regression revealed that Aridity Index helps to minimize the regional spatial variability in *Te* estimates and makes the model geographically consistent.

In addition, the reservoir operating schemes and mechanisms, and timing of sediment release or flushing by the dam may act as important variables that govern *Te* (Brandt, 2000; Kondolf et al., 2014a). However, incorporating these aspects into *Te* calculations is difficult due to data limitations, difficultly in predicting the timing of these mechanisms, and complexity in incorporating it to trapping calculations. In this regard, the age of the dam as an explanatory variable may serve as a proxy, as newer dams tend to include sediment release mechanisms. However, dam age was found not to be a significant contributor to *Te* in this analysis.

Dam height, reservoir length parameters, and Aridity Index are widely available or can be extracted from existing datasets. Sediment fluxes into the reservoir and, in some cases, outgoing

discharge are more challenging to obtain. It may be possible in the future to measure outgoing discharge based on satellite approaches as well (Gleason and Durand, 2020), especially after the launch of the Surface Water and Ocean Topography (SWOT) mission (Biancamaria et al., 2016). To overcome the challenge of obtaining sediment data, a second model was developed using only widely available data to facilitate a wide range of applications:

$$Te = -33.63 - 25.34\log(Q_{out}) + 21.74\log(H) + 19.08\log(D) + 0.21\,L \quad (3)$$

where D is drainage area (km^2). Although this equation has a lower predictive accuracy compared to the previous equation (R^2=0.59; Adj. R^2=0.57; RMSE = 18.1%), it can provide *Te* estimates for the US with reasonable accuracy for data-limited locations.

A machine learning model development was also attempted. In machine learning techniques, large datasets help to learn 'hidden' patterns from the data and therefore have the potential to achieve higher accuracies than simple statistical methods (Lin et al., 2020). However, machine learning techniques are generally suitable for large datasets. The best Random Forest model developed in this analysis yielded an R^2 of 0.50 using all the explanatory variables with an RMSE of 19.72%. The Multi-Layer Perceptron model only achieved a predictive power of 0.22 in terms of R^2 with an RMSE of 24.64%. The relatively small training dataset available in this study likely hindered the development of a robust machine learning model.

3.5. Global *Te* Model

We developed a third model for global-scale applications based on data from the commonly used Global Reservoir and Dam (GRanD) dataset (Lehner et al., 2011b). In addition to the remote sensing-derived *Te* of the 116 dams in the CONUS, 42 additional observed *Te* values outside the US were used to develop this model. The resulting model had an R^2=0.45 (Adj. R^2=0.44) and an RMSE of 22% using four explanatory variables:

$$Te = -28.64 - 20.87\log(Q_{out}) + 16.26\log(D) + 24.17\log(L) + 0.19\,H \quad (4)$$

The Geographically Weighted Regression shows that this model is also consistent in geographic space with a uniform distribution of Local R^2, and a random distribution of standard residuals and standard error. Using this equation, *Te* was calculated for 6823 global dams in the GRanD database for which data were available for essential explanatory variables, and dam impoundments fall on the Grill et al. (2019) river network. For 70 GRanD dams that did not have reservoir polygons (e.g., individual dams that do not form reservoirs), a zero *Te* was assigned to indicate no sediment trapping for sediment modeling efforts. In addition, 54 dams primarily built for navigation were also assigned a zero *Te*. The resulting global *Te* dataset (Figure 10) had an average *Te* of 40.57% (Table 2).

Table 2: Descriptive statistics of *Te* values calculated using the global model.

	Number of Reservoirs	**Sum of reservoir capacities (km^3)***	**Mean *Te* (%)**	**Median *Te* (%)**	**Standard deviation *Te* (%)**
Global	**6823**	**6746 (1.0)**	**40.57**	**39.66**	**14.95**
Africa	624	1043.5 (1.67)	49.11	49.35	13.70
Asia	2203	2365.5 (1.07)	38.20	36.52	14.57
Australia and Oceania	234	95.5 (0.41)	42.68	43.76	14.97
Europe	1245	585.4 (0.47)	39.22	39.81	14.18
North America	2177	1734.5 (0.80)	42.14	39.35	15.40
South America	340	922 (2.7)	43.02	42.64	13.17

*the number within parenthesis is the mean reservoir capacity

Continental-scale analysis (Table 2) shows that dams in Africa have the highest average *Te* (49.11%) in agreement with Vörösmarty et al. (2003) likely due to (i) a high proportion of dams in arid regions, (ii) the resulting need to have large reservoir capacities to stabilize highly variable river flows, and (iii) generally low river discharges (Vörösmarty et al., 2003). Asia accounts for the largest number of dams in GRanD and the greatest sum of reservoir capacities but has the lowest average *Te*. The reasons for this may include the location of dams in more humid locations and rivers with high discharge. In addition, a large proportion of dams in humid regions are hydropower dams with shorter water storage times and frequent water releases, which can reduce their *Te*. The continent of North America, with the second highest number of dams in GRanD and second highest cumulative reservoir capacity, has a relatively high average

Te as expected. However, these differences between continents in terms of average and median *Te* are small at this scale.

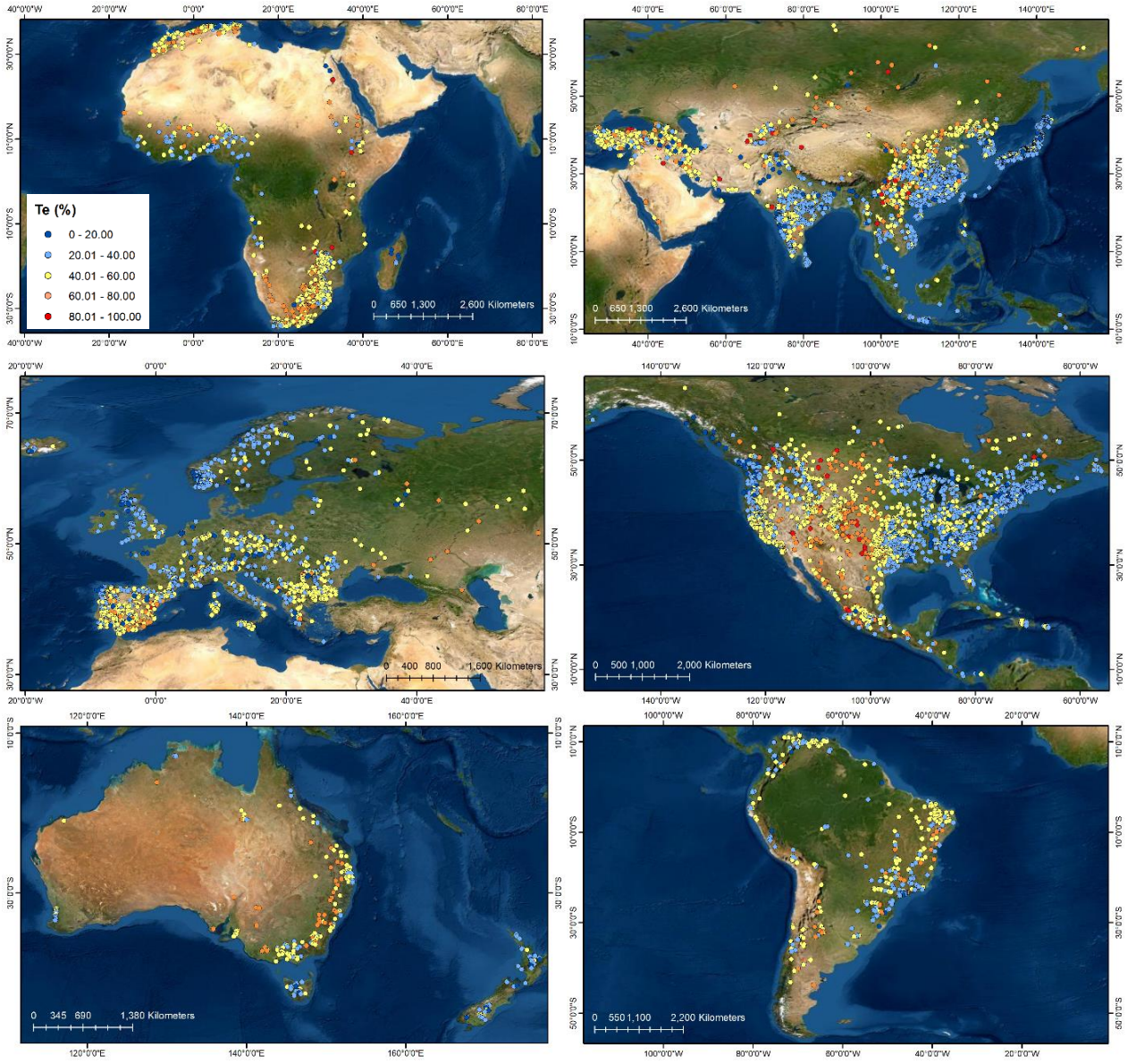

Figure 10: Global distribution of Reservoir *Te* (%) calculated using equation 4 for 6823 dams in the GRanD dataset.

In order to test the regional dependency of *Te*, we tested the explanatory variables to develop an equation only involving dam impoundments in China. *Te* for dams in China can be predicted

with a high accuracy (R^2=0.80; Adj. R^2=0.78; RMSE = 11.25%) using only three variables; log drainage area, log reservoir surface area, and log reservoir capacity. The equation is as follows,

$$Te = 230.44 - 43.3\log(D) + 20.21\log(S) + 29.24\log(SA) \quad (5)$$

where S is storage capacity of the reservoir (km^3), and SA is reservoir surface area (km^2). The negative relationship that upstream drainage area (D) has with *Te* in this model can be explained by the negative relationship between Q and *Te* in the global model as well as the CONUS model. In regional settings, Q and D tend to have a strong correlation. This may also be indicative of the fact that large rivers with large drainage areas can have smaller *Te* values in this region.

These different models for different regions indicate that *Te* may have a strong regional dependency and it may be more accurate to develop regional models (for regions smaller than continental scale) or calibrations for different settings. Some of the reasons for this regional dependency may include climate, river flow regimes, and dam type and operation. Our global *Te* model has a relatively lower predictive capability compared to the CONUS *Te* model, largely due to data limitations. The remote sensing SSC dataset used here for the CONUS is currently in the process of being expanded globally. Once this product is available, observed *Te* can be calculated for global dams, allowing us to develop more robust empirical models for predicting global *Te* and potentially use machine learning techniques.

4. Conclusions

As a major driver of anthropogenic disturbance of fluvial fluxes, the impact of damming on freshwater and coastal systems is key for reliably predicting modern and future sediment dynamics. Scarcity in sediment monitoring has limited the accuracy and universal applicability of sediment trapping parameterization in hydro-geomorphic models. Emerging remote sensing approaches now provide sediment concentration data at large spatial scales, offering unparalleled opportunities to improve our understanding of river sediment transport dynamics. Using such a dataset, we developed a new empirical model for calculating *Te* of US and global reservoirs, based on dam, riverine, and basin attributes. The simplicity of the models will allow modelers to easily incorporate them into their fluvial sediment models, potentially considerably improving

776 the models' ability to represent the effects of anthropogenic activities on sediment dynamics. We
777 also argue that remote sensing-based *Te* calculations can be particularly useful for large-scale
778 hydrological models to represent the trapping efficiencies of reservoirs more realistically than
779 currently available methods derived using theoretical approaches, given that remote-sensing can
780 capture the sediment flux downstream of the dams more accurately.
781
782 In order to test how well remote sensing-captured surface sediment loads represent depth-
783 averaged sediment loads of rivers, a comparison between USGS measured sediment fluxes and
784 remote sensing-calculated sediment fluxes was conducted for 36 gaging stations. The results
785 showed that, with an adjustment factor of 4.45, remote sensing-derived sediment strongly
786 aligned with in-situ observations. In this study, we calculated *Te* for 116 individual dam
787 impoundments across the US using remote sensing observations of long-term sediment data and
788 used that to develop data-driven CONUS and global models to predict *Te*. When compared with
789 the *Te* calculated by previous methods, remote sensing data reveal that large reservoirs can have
790 a wide range of *Te* values, and reservoir volume (indicated by storage capacity) does not
791 necessarily play an important role in determining sediment trapping. This is contrary to the
792 previous claims that *Te* is very large for large reservoirs and small for small reservoirs.
793
794 The development of regional and global models to predict *Te* revealed that regional models
795 better predict *Te*, but global *Te* estimates are possible and can be used in global sediment
796 transport modeling. We found that reservoir, climate, and fluvial sediment flux metrics are
797 important controls of *Te* in both regional and global models. Moving forward, *Te* predictions
798 could benefit from more site-specific and regional information (e.g., climate).
799
800 Future work will include the implementation of the developed sediment trapping model within
801 the WBMsed hydro-geomorphic modeling framework (Cohen et al., 2013, 2014). WBMsed is a
802 spatially and temporally explicit global-scale model with a robust hydrological framework and
803 well-established sediment modules. WBMsed *Te* module is currently based on the Vörösmarty et
804 al. (2003) model. With forthcoming global remote sensing products of SSC, *Te* may also be
805 dynamically assimilated directly for a large dataset of global dams. Improving the representation
806 of sediment trapping in hydro-geomorphic models will aid in predicting current and future river

sediment transport, quantifying the global sediment delivery into the ocean, studying ecological impacts associated with sediment in freshwater systems, and understanding anthropogenic influences on riverine fluxes.

Data Availability Statement

The remote sensing river sediment dataset used for this study is available at https://doi.org/10.5281/zenodo.4900563.

Acknowledgments

This project was funded by a grant from the Alabama Water Institute (AWI; University of Alabama) Interdisciplinary Innovations Program. We thank Jida Wang for providing the encryption key to associate ICOLD dam attribute data with the GeoDAR database.

References

Best, J. and Darby, S.E. (2020). The Pace of Human-Induced Change in Large Rivers: Stresses, Resilience, and Vulnerability to Extreme Events. *One Earth*, *2*(6), pp.510-514.

Best, J. (2019). Anthropogenic stresses on the world's big rivers. *Nature Geoscience*, *12*(1), pp.7-21.

Biancamaria, S., Lettenmaier, D., & Pavelsky, T. (2016). The SWOT Mission and Its Capabilities for Land Hydrology. *Surveys in Geophysics*, *37*(2), 307-337.

Biswas, A.K. and Tortajada, C. (2012). Impacts of the high Aswan Dam. In *Impacts of large dams: A global assessment* (pp. 379-395). Springer, Berlin, Heidelberg.

Blanchard, R.A., Ellison, C.A., Galloway, J.M., and Evans, D.A. (2011), Sediment concentrations, loads, and particle- size distributions in the Red River of the North and selected tributaries near Fargo, North Dakota, during the 2010 spring high-flow event: U.S. Geological Survey Scientific Investigations Report 2011–5064.

Borland, W.M. (1971). Reservoir sedimentation. In Shen, H.W., editor, River mechanics. Vol. II, Fort Collins, CO: Colorado State University, 29.1–29.38.

Brandt, S. A. (2000). Classification of geomorphological effects downstream of dams. *Catena*, *40*(4), 375-401.

Brown, C.B. (1943). Discussion of Sedimentation in reservoirs, by J. Witzig. Proceedings of the American Society of Civil Engineers 69, 1493–1500.

Brune, G.M. (1953). Trap efficiency of reservoirs. Eos, Transactions American Geophysical Union, 34(3), pp.407-418.

Chakrapani, G. J. (2005). Factors controlling variations in river sediment loads. Current science, 569-575.

Chen, C. (1975). Design of sediment retention basins. In Proceedings, national symposium on urban hydrology and sediment control, July, Lexington, KY: University of Kentucky, 285–98.

Churchill, M.A. (1948). Discussion of Analyses and use of reservoir sedimentation data by L.C. Gottschalk. In Proceedings of the federal inter- agency sedimentation conference, Denver, Colorado, Washington, DC: US Geological Survey, 139–40.

Cohen, S., Kettner, A.J., Syvitski, J.P. and Fekete, B.M. (2013). WBMsed, a distributed global-scale riverine sediment flux model: Model description and validation. *Computers & Geosciences*, *53*, pp.80-93.

Cohen, S., Kettner, A.J. and Syvitski, J.P. (2014). Global suspended sediment and water discharge dynamics between 1960 and 2010: Continental trends and intra-basin sensitivity. *global and planetary change*, *115*, pp.44-58.

Dethier, E.N., Renshaw, C.E. and Magilligan, F.J. (2020). Toward improved accuracy of remote sensing approaches for quantifying suspended sediment: Implications for suspended-sediment monitoring. Journal of Geophysical Research: Earth Surface, 125(7), p.e2019JF005033.

Dunn, F.E., Darby, S.E., Nicholls, R.J., Cohen, S., Zarfl, C. and Fekete, B.M. (2019). Projections of declining fluvial sediment delivery to major deltas worldwide in response to climate change and anthropogenic stress. *Environmental Research Letters*, *14*(8), p.084034.

Espinosa-Villegas, C. O., & Schnoor, J. L. (2009). Comparison of long-term observed sediment trap efficiency with empirical equations for Coralville Reservoir, Iowa. *Journal of Environmental Engineering*, *135*(7), 518-525.

ESRI, (2021). USA Detailed Water Bodies layer package for ArcGIS (downloaded from https://www.arcgis.com/home/item.html?id=84e780692f644e2d93cefc80ae1eba3a)

Fagundes, H.O, de Paiva, R.C.D., Fan, F.M., Buarque, D.C. and Fassoni-Andrade, A.C. (2020). Sediment modeling of a large-scale basin supported by remote sensing and in-situ observations. *Catena*, *190*, p.104535.

Gardner, J. R., Yang, X., Topp, S. N., Ross, M. R. V., Altenau, E. H., & Pavelsky, T. M. (2021). The color of rivers. Geophysical Research Letters, 48, e2020GL088946. https://doi. org/10.1029/2020GL088946.

886 Gardner, J., Pavelsky, T., Yang, X., Topp, S., & Ross, M. (2022). River Sediment Database
887 (RiverSed) (v1.0.0) [Data set]. Zenodo. https://doi.org/10.5281/zenodo.4900563

888 Gleason, C. J., & Durand, M. T. (2020). Remote sensing of river discharge: a review and a
889 framing for the discipline. *Remote Sensing*, *12*(7), 1107.

890 Grill, G., Lehner, B., Thieme, M., Geenen, B., Tickner, D., Antonelli, F., Babu, S., Borrelli, P.,
891 Cheng, L., Crochetiere, H. and Macedo, H.E. (2019). Mapping the world's free-flowing
892 rivers. *Nature*, *569*(7755), pp.215-221.

893 Haddeland, I., Heinke, J., Biemans, H., Eisner, S., Flörke, M., Hanasaki, N., Konzmann, M.,
894 Ludwig, F., Masaki, Y., Schewe, J. and Stacke, T. (2014). Global water resources affected by
895 human interventions and climate change. Proceedings of the National Academy of
896 Sciences,111(9), pp.3251-3256.

897 Heinemann, H.G. (1984). Reservoir trap efficiency. In Hadley, R.F. and Walling, D.E., editors,
898 Erosion and sediment yield: some methods of measurement and modelling, Norwich:
899 GeoBooks, 201–18.
900
901 Hu, B., Yang, Z., Wang, H., Sun, X., Bi, N. and Li, G. (2009). Sedimentation in the Three
902 Gorges Dam and the future trend of Changjiang (Yangtze River) sediment flux to the
903 sea. *Hydrology and Earth System Sciences*, *13*(11), pp.2253-2264.
904
905 Jothiprakash, V. and Vaibhav, G.A.R.G. (2008). Re-look to conventional techniques for trapping
906 efficiency estimation of a reservoir. *International Journal of Sediment Research*, *23*(1),
907 pp.76-84.
908
909 Kondolf, G.M., Gao, Y., Annandale, G.W., Morris, G.L., Jiang, E., Zhang, J., Cao, Y., Carling,
910 P., Fu, K., Guo, Q. and Hotchkiss, R. (2014a). Sustainable sediment management in
911 reservoirs and regulated rivers: Experiences from five continents. *Earth's Future*, *2*(5),
912 pp.256-280.

913 Kondolf, G.M., Rubin, Z.K. and Minear, J.T. (2014b). Dams on the Mekong: Cumulative
914 sediment starvation. *Water Resources Research*, *50*(6), pp.5158-5169.
915
916 Kummu, M., Lu, X. X., Wang, J. J., & Varis, O. (2010). Basin-wide sediment trapping efficiency
917 of emerging reservoirs along the Mekong. *Geomorphology*, *119*(3-4), 181-197.
918
919 Laguionie, P., Crave, A. and Jigorel, A. (2007). Velocity and suspended sediment concentration
920 profiles in rivers: in situ measurements and flux modelling. *WIT Transactions on Ecology*
921 *and the Environment*, *104*, pp.335-343.
922
923 Latrubesse, E.M., Arima, E.Y., Dunne, T., Park, E., Baker, V.R., d'Horta, F.M., Wight, C.,
924 Wittmann, F., Zuanon, J., Baker, P.A. and Ribas, C.C. (2017). Damming the rivers of the
925 Amazon basin. *Nature*, *546*(7658), pp.363-369.

926 Lehner, B., Liermann, C.R., Revenga, C., Vörösmarty, C., Fekete, B., Crouzet, P., Döll, P.,
927 Endejan, M., Frenken, K., Magome, J. and Nilsson, C. (2011a). High-resolution mapping of
928 the world's reservoirs and dams for sustainable river-flow management. *Frontiers in Ecology*
929 *and the Environment*, *9*(9), pp.494-502.

930 Lehner, B., Liermann, C.R., Revenga, C., Vörösmarty, C., Fekete, B., Crouzet, P., Döll, P.,
931 Endejan, M., Frenken, K., Magome, J. and Nilsson, C. (2011b). Global reservoir and dam
932 (grand) database. *Technical Documentation, Version*, *1*, pp.1-14.

933 Lewis, S.E., Bainbridge, Z.T., Kuhnert, P.M., Sherman, B.S., Henderson, B., Dougall, C.,
934 Cooper, M. and Brodie, J.E. (2013). Calculating sediment trapping efficiencies for reservoirs
935 in tropical settings: a case study from the Burdekin Falls Dam, NE Australia. *Water*
936 *Resources Research*, *49*(2), pp.1017-1029.

937 Li, L., Ni, J., Chang, F., Yue, Y., Frolova, N., Magritsky, D., Borthwick, A.G., Ciais, P., Wang,
938 Y., Zheng, C. and Walling, D.E. (2020). Global trends in water and sediment fluxes of the
939 world's large rivers. *Science Bulletin*, *65*(1), pp.62-69.

940 Lin, P., Pan, M., Allen, G.H., de Frasson, R.P., Zeng, Z., Yamazaki, D. and Wood, E.F. (2020).
941 Global estimates of reach-level bankfull river width leveraging big data geospatial
942 analysis. *Geophysical Research Letters*, *47*(7), p.e2019GL086405.

943 Lu, X.X., Ran, L.S., Liu, S., Jiang, T., Zhang, S.R. and Wang, J.J. (2013). Sediment loads
944 response to climate change: A preliminary study of eight large Chinese rivers. *International*
945 *Journal of Sediment Research*, *28*(1), pp.1-14.

946 McKay, L., Bondelid, T., Dewald, T., Rea, A., Johnston, C. and Moore, R. (2015). NHDPlus
947 version 2: user guide (data model version 2.1). *Horizon Systems*.

948 Merritt, W.S., Letcher, R.A. and Jakeman, A.J. (2003). A review of erosion and sediment
949 transport models. *Environmental modelling & software*, *18*(8-9), pp.761-799.

950 Moore, R.B., McKay, L.D., Rea, A.H., Bondelid, T.R., Price, C.V., Dewald, T.G., and Johnston,
951 C.M. (2019). User's guide for the national hydrography dataset plus (NHDPlus) high
952 resolution: U.S. Geological Survey Open-File Report 2019– 1096, 66 p.,
953 https://doi.org/10.3133/ofr20191096.

954 Mulligan, M., van Soesbergen, A. and Sáenz, L. (2020). GOODD, a global dataset of more than
955 38,000 georeferenced dams. *Scientific Data*, *7*(1), pp.1-8.

956 Narayanan, A. (2022). Sediment Response to Deforestation in the Amazon River Basin. Master's
957 Thesis, University of Alabama, USA.

958 Overeem, I., Hudson, B.D., Syvitski, J.P., Mikkelsen, A.B., Hasholt, B., Van Den Broeke, M.R.,
959 Noël, B.P.Y. and Morlighem, M. (2017). Substantial export of suspended sediment to the
960 global oceans from glacial erosion in Greenland. Nature Geoscience, 10(11), pp.859-863.

961 Pelletier, J.D. (2012). A spatially distributed model for the long-term suspended sediment
962 discharge and delivery ratio of drainage basins. *Journal of Geophysical Research: Earth*
963 *Surface*, *117*(F2).
964
965 Rausch, D.L. and Heinemann, H.G. (1975). Controlling reservoir trap efficiency. *Transactions of*
966 *the ASAE*, *18*(6), pp.1105-1108.
967
968 Rausch, D.L. and Schreiber, J.D. (1981). *Sediment and nutrient trap efficiency of a small flood-*
969 *detention reservoir* (Vol. 10, No. 3, pp. 288-293). American Society of Agronomy, Crop
970 Science Society of America, and Soil Science Society of America.
971
972 Rodgers, K.D. (2017). A Reservoir Morphology Database for the Conterminous United States:
973 U.S. Geological Survey data release, https://doi.org/10.5066/F7GF0RQZ

974 Schmidt, J.C. and Wilcock, P.R. (2008). Metrics for assessing the downstream effects of
975 dams. *Water Resources Research*, *44*(4).
976
977 Sharma, D.K., Sharma, S.K. and Suri, S. (2018). Sediment Management of Projects on
978 Himalayan Rivers-A Case Study of Bhakra Dam and Beas Sutlej Link Project. *INCOLD*
979 *Journal (A Half Yearly Technical Journal of Indian Committee on Large Dams)*, *7*(2), pp.3-
980 8.
981
982 Syvitski, J. P. (2003). Supply and flux of sediment along hydrological pathways: research for the
983 21st century. *Global and Planetary Change*, *39*(1-2), 1-11.
984
985 Syvitski, J. P., Vörösmarty, C. J., Kettner, A. J., & Green, P. (2005). Impact of humans on the
986 flux of terrestrial sediment to the global coastal ocean. *science*, *308*(5720), 376-380.
987
988 Syvitski, J., Ángel, J. R., Saito, Y., Overeem, I., Vörösmarty, C. J., Wang, H., & Olago, D.
989 (2022). Earth's sediment cycle during the Anthropocene. Nature Reviews Earth &
990 Environment, 3(3), 179-196.
991
992 Syvitski, J.P. and Kettner, A. (2011). Sediment flux and the Anthropocene. *Philosophical*
993 *Transactions of the Royal Society A: Mathematical, Physical and Engineering*
994 *Sciences*, *369*(1938), pp.957-975.

995 Syvitski, J.P., Milliman, J.D. (2007). Geology, geography, and humans battle for dominance over
996 the delivery of fluvial sediment to the coastal ocean. J. Geol.115 (1), pp.1–19.

997 Tan, G., Chen, P., Deng, J., Xu, Q., Tang, R., Feng, Z., & Yi, R. (2019). Review and
998 improvement of conventional models for reservoir sediment trapping
999 efficiency. *Heliyon*, *5*(9), e02458.
1000
1001 USDA-SCS, (1983). National engineering hand- book (2nd edn) (Section 3: 'Sedimentation';
1002 Chapter 8 'Sediment storage design criteria') Washington, DC: US Department of
1003 Agriculture.

Trabucco, A. and Zomer, R.J. (2019). Global aridity index and potential evapotranspiration (ET0) climate database v2. *CGIAR Consort Spat Inf*, *10*, p.m9.

Vercruysse, K., Grabowski, R.C. and Rickson, R.J. (2017). Suspended sediment transport dynamics in rivers: Multi-scale drivers of temporal variation. *Earth-Science Reviews*, *166*, pp.38-52.

Verstraeten, G. and Poesen, J. (2000). Estimating trap efficiency of small reservoirs and ponds: methods and implications for the assessment of sediment yield. *Progress in Physical Geography*, *24*(2), pp.219-251.

Vörösmarty, C.J., Meybeck, M., Fekete, B., Sharma, K., Green, P., Syvitski, J.P.M. (2003). Anthropogenic sediment retention: major global impact from registered river impoundments. Glob. Planet. Chang. 39 (1–2), pp.169–190.

Wada, Y., de Graaf, I.E. and van Beek, L.P. (2016). High-resolution modeling of human and climate impacts on global water resources. *Journal of Advances in Modeling Earth Systems*, *8*(2), pp.735-763.

Walling, D.E. (2012). The role of dams in the global sediment budget. *IAHS-AISH publication*, pp.3-11.

Wang, K., Gelda, R.K., Mukundan, R. and Steinschneider, S. (2021a). Inter-model Comparison of Turbidity-Discharge Rating Curves and the Implications for Reservoir Operations Management. *JAWRA Journal of the American Water Resources Association*, *57*(3), pp.430-448.

Wang, J., Walter, B.A., Yao, F., Song, C., Ding, M., Maroof, A.S., Zhu, J., Fan, C., Xin, A., McAlister, J.M. and Sikder, S. (2021b). GeoDAR: Georeferenced global dam and reservoir dataset for bridging attributes and geolocations. Earth System Science Data Discussions, pp.1-52.

Wei, X., Sauvage, S., Ouillon, S., Le, T. P. Q., Orange, D., Herrmann, M., & Sanchez-Perez, J. M. (2021). A modelling-based assessment of suspended sediment transport related to new damming in the Red River basin from 2000 to 2013. *Catena*, *197*, 104958.

Wohl, E. and Rathburn, S. (2003). Mitigation of sedimentation hazards downstream from reservoirs. *International Journal of Sediment Research*, *18*(2), pp.97-106.

Williams, G.P. and Wolman, M.G. (1984). *Downstream effects of dams on alluvial rivers* (Vol. 1286). US Government Printing Office.

Wu, Z., Zhao, D., Syvitski, J.P., Saito, Y., Zhou, J. and Wang, M. (2020). Anthropogenic impacts on the decreasing sediment loads of nine major rivers in China, 1954–2015. *Science of the Total Environment*, *739*, p.139653.

1048 Yang, X., Pavelsky, T.M., Ross, M.R., Januchowski-Hartley, S.R., Dolan, W., Altenau, E.H.,
1049 Belanger, M., Byron, D., Durand, M., Van Dusen, I. and Galit, H. (2022). Mapping flow-
1050 obstructing structures on global rivers. Water Resources Research, 58(1),
1051 p.e2021WR030386.

1052 Zarfl, C., Lumsdon, A.E., Berlekamp, J., Tydecks, L., and Tockner, K. (2015). A global boom in
1053 hydropower dam construction. Aquat. Sci. 77, 161–171, https://doi.org/10. 1007/s00027-014-
1054 0377-0.

Supplementary materials

Table S1: USGS gage observations (O-) used for validation of suspended sediment flux (Qs) and discharge (Q)

ID	USGS site #	Lat	Lon	Area (km^2)	USGS O-Qs time period	USGS O-Qs (kg/s)	USGS O-Q (m^3/s)	Remote sensing Qs (kg/s)	NHDplus Q (m^3/s)
1	01357500	42.79	-73.71	8,935	2003-2018	15.05	179.84	3.99	171.91
2	06486000	42.49	-96.41	814,811	1992-2019	257.31	909.59	40.53	1066.60
3	06610000	41.26	-95.92	836,049	1992-2019	476.65	1056.64	65.95	1065.09
4	06807000	40.68	-95.85	1,061,896	1992-2019	736.73	1259.21	118.54	1262.72
5	01331095	42.94	-73.65	9,772	1992-2001	2.61	198.59	2.05	183.99
6	05587455	38.95	-90.37	443,665	1990-2016	690.98	3665.79	204.44	3681.30
7	12340500	46.88	-113.93	15,594	1989-2016	3.65	79.48	1.14	83.65
8	07020500	37.90	-89.83	1,835,267	1988-2016	2659.89	6810.37	638.16	6483.72
9	04193500	41.50	-83.71	16,395	1988-2003	36.70	171.62	11.46	157.98
10	02489500	30.79	-89.82	17,024	1986-1993	39.20	284.70	15.35	330.61
11	05474000	40.75	-91.28	11,168	1985-2019	64.06	100.35	7.37	90.94
12	06452000	43.75	-99.56	25,680	1985-2019	111.70	21.61	3.08	17.83
13	05465500	41.18	-91.18	32,375	1985-2019	74.09	313.70	12.19	282.50
14	11303500	37.68	-121.27	35,066	1985-2019	7.79	108.86	3.68	134.60
15	08330000	35.09	-106.68	45,169	1985-2019	28.16	33.52	7.76	39.21
16	08332010	34.42	-106.80	49,806	1985-2019	24.67	28.87	5.86	27.66
17	08354900	34.26	-106.89	69,334	1985-2019	81.17	29.15	5.99	26.07
18	08358400	33.68	-107.00	71,743	1985-2019	71.14	22.33	9.30	24.72
19	11447650	38.46	-121.50	nan	1985-2019	41.72	587.21	15.39	749.23
20	05325000	44.17	-94.00	38,591	1985-2017	46.22	186.17	5.35	141.84
21	07010000	38.63	-90.18	1,805,223	1985-2017	2642.23	6522.81	572.56	6194.66
22	07022000	37.22	-89.46	1,847,181	1985-2017	2557.32	7081.22	658.07	6699.36
23	05586100	39.70	-90.65	69,264	1985-2011	170.20	740.62	39.04	722.86
24	05481650	41.68	-93.67	15,128	1985-2004	5.63	114.59	2.24	110.19
25	04198000	41.31	-83.16	3,240	1985-2002	7.62	36.61	2.44	33.25
26	05288500	45.13	-93.30	49,469	1985-1996	7.84	284.49	4.21	272.13
27	02116500	35.86	-80.39	5,905	1985-1994	20.40	82.78	4.81	91.75
28	09364500	36.72	-108.20	3,522	1985-1993	13.19	22.66	1.63	25.67
29	09217000	41.52	-109.45	36,260	1985-1992	3.16	41.63	1.28	53.22
30	01638500	39.27	-77.54	24,996	1985-1991	35.13	286.29	7.15	301.42
31	06115200	47.63	-108.69	105,281	1985-1991	138.49	231.88	23.02	268.70
32	06329500	47.68	-104.16	178,966	1985-1991	206.37	320.78	54.76	353.50

33	01567000	40.48	-77.13	8,687	1985-1990	2.83	127.17	2.63	130.88
34	05454500	41.66	-91.54	8,472	1985-1987	8.45	79.30	2.06	71.13
35	09368000	36.78	-108.68	33,411	1985-1986	108.66	47.48	4.61	61.73
36	12334550	46.83	-113.81	9,472	1986-2016	1.61	37.22	0.85	40.15

1059